nature chemistry

ARTICLES

https://doi.org/10.1038/s41557-020-00629-3

Check for updates

Direct observation of coherent femtosecond solvent reorganization coupled to intramolecular electron transfer

Elisa Biasin[1]✉, Zachary W. Fox[2], Amity Andersen[3], Kathryn Ledbetter[1], Kasper S. Kjær[1,4], Roberto Alonso-Mori[5], Julia M. Carlstad[2,10], Matthieu Chollet[5], James D. Gaynor[2,10], James M. Glownia[5], Kiryong Hong[6,11], Thomas Kroll[5], Jae Hyuk Lee[6,12], Chelsea Liekhus-Schmaltz[2], Marco Reinhard[1], Dimosthenis Sokaras[5], Yu Zhang[7,13], Gilles Doumy[8], Anne Marie March[8], Stephen H. Southworth[8], Shaul Mukamel[7], Kelly J. Gaffney[1], Robert W. Schoenlein[1,5], Niranjan Govind[9]✉, Amy A. Cordones[1]✉ and Munira Khalil[2]✉

It is well known that the solvent plays a critical role in ultrafast electron-transfer reactions. However, solvent reorganization occurs on multiple length scales, and selectively measuring short-range solute–solvent interactions at the atomic level with femtosecond time resolution remains a challenge. Here we report femtosecond X-ray scattering and emission measurements following photoinduced charge-transfer excitation in a mixed-valence bimetallic ($Fe^{II}Ru^{III}$) complex in water, and their interpretation using non-equilibrium molecular dynamics simulations. Combined experimental and computational analysis reveals that the charge-transfer excited state has a lifetime of 62 fs and that coherent translational motions of the first solvation shell are coupled to the back electron transfer. Our molecular dynamics simulations identify that the observed coherent translational motions arise from hydrogen bonding changes between the solute and nearby water molecules upon photoexcitation, and have an amplitude of tenths of ångströms, 120–200 cm^{-1} frequency and ~100 fs relaxation time. This study provides an atomistic view of coherent solvent reorganization mediating ultrafast intramolecular electron transfer.

Ultrafast photoinduced electron-transfer reactions are the key steps governing natural and artificial energy conversion processes and are therefore the subject of intense experimental and theoretical studies across several fields of chemistry[1]. A thorough understanding of electron transfer in the condensed phase requires detailing the complex couplings between electronic and atomic degrees of freedom in the solute and the surrounding solvent[2–6]. Femtosecond electronic and vibrational spectroscopic studies have shown that solute–solvent dynamics critically affect the energetics and the rates of electron transfer[7,8]. However, the role of specific solute–solvent interactions in ultrafast electron-transfer processes remains largely unexplored. This is because time-resolved optical spectroscopy methods measure the solvent reorganization energy in response to a change in electronic charge distribution, often termed dielectric solvation, by averaging over all length scales in the solvent response and thus obscuring the detailed nature of the specific solute–solvent interactions [9–12]. In particular, time-resolved fluorescence Stokes shift measurements have been used extensively to investigate dielectric solvation and have been found to report mostly on the dipolar solvent response[9,10,13]. Time-resolved nonlinear infrared spectroscopy techniques have advanced our understanding of solute–solvent interactions, but separating the effects of inter- and intramolecular interactions on experimental observables is demanding, making it difficult to connect solvation dynamics to changes in the vibrational spectrum[14–17]. To date, an atomic level mechanistic understanding of solvation dynamics upon electron transfer has been derived primarily from molecular dynamics (MD) simulations[13,18–21]. Femtosecond X-ray pulses available at X-ray free electron lasers (XFELs) provide a powerful new tool to monitor the photoinduced ultrafast motions of electrons and nuclei in solvated molecular systems. In particular, time-resolved X-ray solution scattering (XSS) at XFELs directly probes, at the atomic spatial and temporal scales, the photoinduced changes of all the atom-pair distances[22,23]. These observables can be directly compared with the atomic positions calculated by MD simulations, enabling direct tracking of photoinduced structural dynamics and the accompanying changes in the solvation shell structure[24–26]. In this work, we use femtosecond XSS, in combination with non-equilibrium MD

[1]Stanford PULSE Institute, SLAC National Accelerator Laboratory, Menlo Park, CA, USA. [2]Department of Chemistry, University of Washington, Seattle, WA, USA. [3]Environmental Molecular Sciences Division, Earth and Biological Sciences Directorate, Pacific Northwest National Laboratory, Richland, WA, USA. [4]Department of Physics, Technical University of Denmark, Kongens Lyngby, Denmark. [5]Linac Coherent Light Source, SLAC National Accelerator Laboratory, Menlo Park, CA, USA. [6]Ultrafast X-ray Science Laboratory, Chemical Sciences Division, Lawrence Berkeley National Laboratory, Berkeley, CA, USA. [7]Department of Chemistry, Physics, and Astronomy, University of California, Irvine, CA, USA. [8]Chemical Sciences and Engineering Division, Argonne National Laboratory, Lemont, IL, USA. [9]Physical Sciences Division, Physical and Computational Sciences Directorate, Pacific Northwest National Laboratory, Richland, WA, USA. [10]Present address: Department of Chemistry, University of California, Berkeley, CA, USA. [11]Present address: Gas Metrology Group, Division of Chemical and Biological Metrology, Korea Research Institute of Standards and Science, Daejeon, Republic of Korea. [12]Present address: Pohang Accelerator Laboratory, Pohang, Republic of Korea. [13]Present address: Q-Chem, Pleasanton, CA, USA. ✉e-mail: ebiasin@stanford.edu; niri.govind@pnnl.gov; acordon@stanford.edu; mkhalil@uw.edu

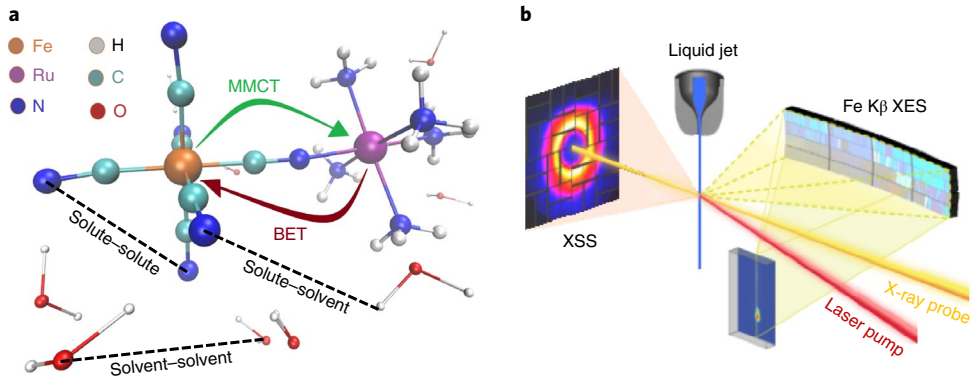

Fig. 1 | Mixed-valence complex under study and experimental set-up. a, FeRu molecule in water; 800 nm excitation induces MMCT from the Fe to the Ru centre, followed by ultrafast BET. The interatomic distances probed by the elastically scattered X-rays are classified into solute–solute (intramolecular), solute–solvent and solvent–solvent atom-pair distances. **b**, Schematic of the experimental set-up: a combination of a large area detector and a von Hamos emission spectrometer allows for the detection of both elastic scattering and the Fe Kβ fluorescence as a function of laser-pump/X-ray-probe time delay. Figure adapted with permission from ref. [37], RSC.

simulations, to provide a real space picture of short-range, specific solvent motions coupled to electron transfer. Our results fill in an important knowledge gap in our understanding of electron-transfer reactions in solution.

Cyanide-bridged mixed-valence transition metal complexes, like $[NC Fe^{II}(CN)_5(NH_3)_5 Ru^{III}]^-$ (FeRu; Fig. 1a), have served as invaluable platforms for advancing our understanding of electron-transfer reactions[1,3,8]. In these systems, the metal-to-metal charge-transfer (MMCT) excitation is short lived (~100 fs) and followed by ultrafast back electron transfer (BET), and the electronic and nuclear dynamics are strongly coupled, as reported by nonlinear optical, infrared and two-dimensional vibrational electronic spectroscopy experiments[8,27–29]. In FeRu, 800 nm photoexcitation promotes an electron from the Fe to the Ru centre ($Fe^{II}Ru^{III} \rightarrow Fe^{III}Ru^{II}$). Barbara and coworkers observed a BET time of ~89 fs in water and found that this value depends on the solvent[28]. Since the BET timescale was found to be slower in deuterated water, the authors concluded that hydrogenic solvent motions, in particular librations, are directly involved in the electron-transfer process. However, as discussed in a later work by Barbara and coworkers on a complex similar to FeRu (ref. [30]), no direct correlation between librations or other solvent motions and the electron-transfer process could be established, since disentangling the spectroscopic signatures of vibrational relaxation and solvation dynamics is challenging. How specific solute–solvent interactions affect the photoinduced dynamics of FeRu and related mixed-valence complexes is an important open question. It is well established that both the cyano and amine ligand groups of FeRu support specific hydrogen bonding interactions with the solvent, causing solvatochromic shifts of their charge-transfer absorption bands[31,32], and modulating the vibronic and vibrational couplings of the ligands[33,34]. For FeRu in water, these ligand–solvent hydrogen bonding interactions are expected to be weaker in the MMCT state ($Fe^{III}Ru^{II}$) than in the ground state ($Fe^{II}Ru^{III}$)[35,36]. Changes in the specific solute–solvent interactions of hydrogen-bonding molecules like FeRu cannot be properly accounted for using a simple continuum solvation model, and quantitative experimental measurements of these interactions are indispensable.

To track the photoinduced ultrafast motions of electrons and nuclei coupled to the MMCT excitation of FeRu in water, we use a combination of time-resolved X-ray emission spectroscopy (XES) and XSS (Fig. 1b), as in recent experiments[25,37]. XES in the $1s3p$ $K\beta_{1,3}$ region (Kβ XES) reports on the local Fe oxidation and spin state[38], and therefore provides a real-time measure of the

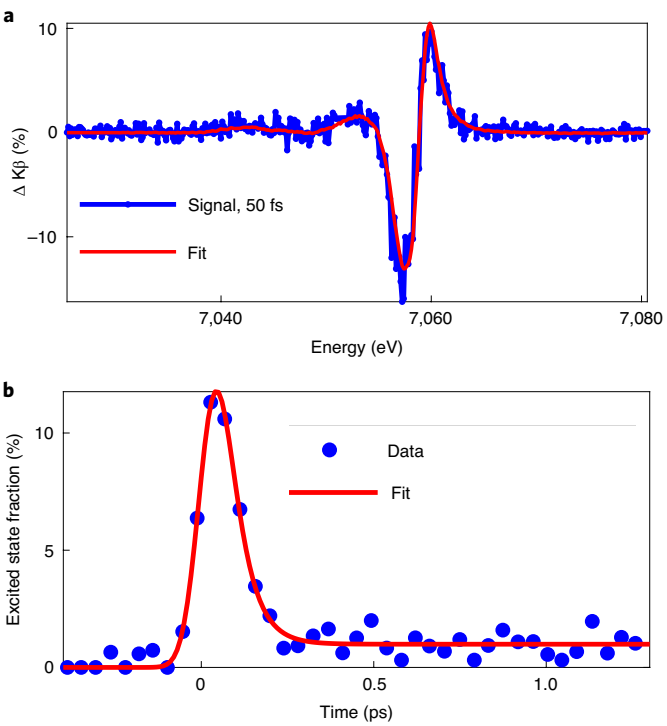

Fig. 2 | Fe Kβ XES tracks the MMCT excited-state population. a, Fe Kβ XES difference spectrum (blue) measured 50 fs after excitation. This spectrum is described by the difference in the measured Kβ XES spectra of Fe(III)- and Fe(II)-hexacyanide (red line). **b**, The time-dependent fraction of molecules in the MMCT state obtained by fitting the reference spectrum to the time-dependent Kβ data. The red line is a fit of an exponential decay with a lifetime of 62 ± 10 fs plus offset, broadened by the instrument response function.

electron-transfer process. The XES measurement can be correlated with the structural information obtained from XSS, since the two signals are recorded simultaneously. By describing the couplings with the solvent through electrostatic interactions in a classical MD framework, we find that the time-dependent XSS signal is dominated by contributions from the water structural reorganization,

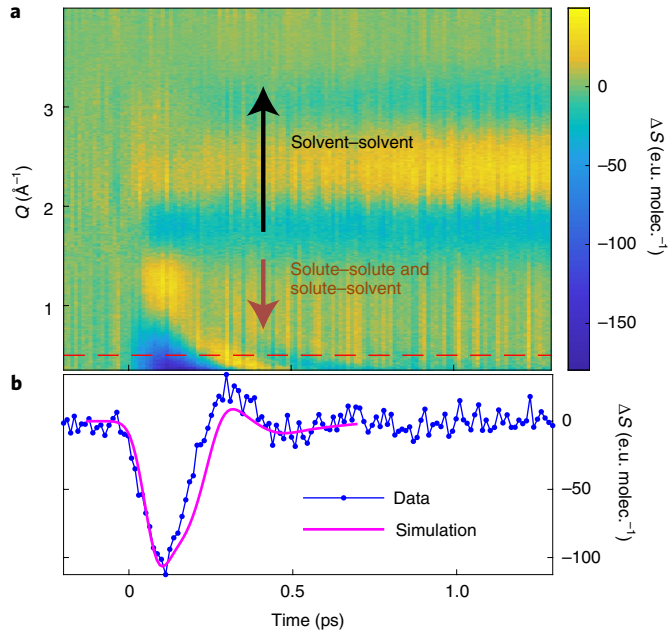

Fig. 3 | The XSS signal. a, Isotropic difference scattering signal measured upon 800 nm excitation of FeRu in water as a function of pump–probe time delay and scattering vector Q. The signal at $Q<1.5$ Å^{-1} arises from changes in intramolecular and solute–solvent distances, while the signal at $Q>1.5$ Å^{-1} reports on the increase in temperature of the water. The magnitude of the signal at $Q=0.5$ Å^{-1} (red dashed line) oscillates as a function of pump–probe time-delay. **b**, Time evolution of both measured and calculated difference scattering signal averaged in a scattering vector range between 0.4 and 0.6 Å^{-1}. The calculated signal is the result of non-equilibrium MD simulations (Fig. 5); e.u. molec.$^{-1}$, electron units per solute molecule.

reflecting large changes in excited-state ligand–solvent interactions and minimal intramolecular structural changes in the excited state of the solute. Ultimately, the combination of femtosecond XSS, XES and MD simulations enables the direct observation of the solute–solvent reorganization dynamics in response to photoinduced MMCT and subsequent BET in FeRu with femtosecond and sub-ångström resolution.

Results and discussion

Ultrafast BET characterized by Fe Kβ XES. Figure 2a shows the Fe Kβ XES difference spectra measured 50 fs after 800 nm excitation of FeRu in water. This signal can be described by a reference spectrum constructed from the difference between the Kβ spectra of $[Fe^{III}(CN)_6]^{3-}$ and $[Fe^{II}(CN)_6]^{4-}$ identifying the changes in electronic structure of FeRu following MMCT excitation. Only the amplitude of the measured Kβ signal shows time dependence (Supplementary Fig. 4), and a fit of the reference spectrum to the entire dataset (Supplementary Discussion 2, equation (1)) yields the MMCT fraction of molecules at each time delay, as shown in Fig. 2b. This signal (blue points) is overlaid with a fit (red line) of an exponential decay starting at time zero, broadened by a Gaussian instrument response function, and summed to an offset (Supplementary Discussion 2, equation (2)). From the fit, we find an initial excitation fraction of 25 ± 4%, 62 ± 10 fs MMCT state lifetime, an instrument response function of ~80 fs (full-width at half-maximum (FWHM)) and a 1% offset. This offset, corresponding to a minor excitation channel, is further discussed in Supplementary Discussion 4. Barbara and coworkers had previously reported a similar BET time (89 ± 10 fs)[28]. The MMCT excited-state lifetime obtained from the analysis of the Fe Kβ XES is used in the interpretation of the XSS data described in the following section.

Ultrafast solute–solvent interactions dominate the XSS signal. Figure 3a shows the isotropic difference scattering signal $\Delta S(Q,t)$ measured upon 800 nm photoexcitation of FeRu as a function of pump–probe time delay t and scattering vector Q. As detailed in previous work[23,39,40], this signal arises from photoinduced changes in the solute–solute, solute–solvent and solvent–solvent atom-pair distances in the sample (examples of which are illustrated in Fig. 1a):

$$\Delta S(Q,t) = \Delta S^{\text{solute-solute}}(Q,t) + \Delta S^{\text{solute-solvent}}(Q,t) + \Delta S^{\text{solvent-solvent}}(Q,t). \quad (1)$$

The difference scattering signal at $Q<1.5$ Å^{-1} arises from changes in solute–solute and solute–solvent distances. In the first 100 fs after excitation, a negative signal develops in the low-Q region (below 0.8 Å^{-1}), which is indicative of an increase of atom-pair distances[23,25]. On the same timescale a positive peak grows in with maximum intensity at ~1.3 Å^{-1} and shifts towards lower Q values with increasing time delay, yielding an oscillatory feature in the time evolution of the low-Q signal. This oscillatory feature is evident in Fig. 3b, which shows a cut at $Q=0.5\pm0.1$ Å^{-1} of the measured difference scattering data. This oscillation is indicative of coherent motion involving an expansion of atom-pair distances and subsequent relaxation to the original value. Since the oscillation period (~390 fs; Supplementary Fig. 8) is not attributable to any intramolecular vibrations, and the short lifetime of the MMCT state precludes large intramolecular structural rearrangements, we tentatively conclude that the low-Q signal is dominated by solvent reorganization. This conclusion is tested below by comparison with MD simulations.

At $Q>1.5$ Å^{-1}, the difference scattering signal develops on the picosecond timescale and has the same Q dependence as the signal measured for water when temperature is increased at constant volume[41]. This signal is the $\Delta S^{\text{solvent-solvent}}(Q,t)$ contribution to equation (1) and provides direct access to the energy transfer from the solute to the solvent. The $\Delta S^{\text{solvent-solvent}}(Q,t)$ component is analysed and

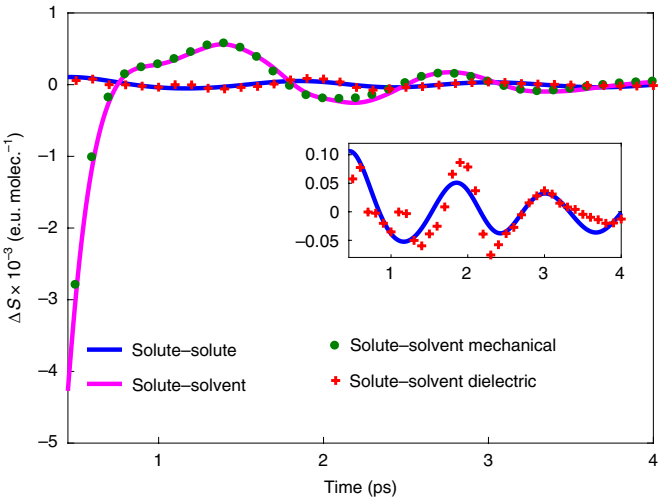

Fig. 4 | Difference scattering signals calculated from equilibrium MD simulations of the GS and MMCT state of FeRu in water. The solute–solute signal (blue line), which arises from changes between the GS and MMCT state TDDFT-calculated FeRu structures, is negligible with respect to the solute–solvent signal (magenta line). The solute–solvent signal arising from changes in solute structure (mechanical, red crosses) is negligible with respect to that arising from the response to changes in solute partial charges (dielectric, green circles).

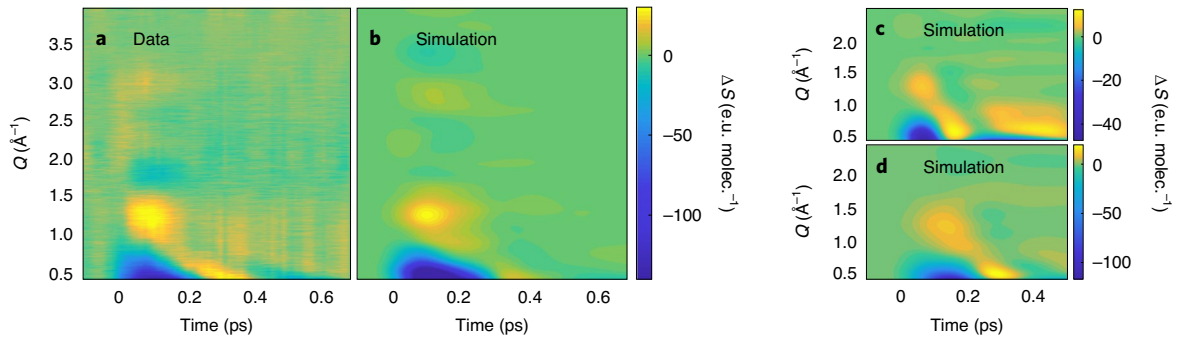

Fig. 5 | Non-equilibrium MD simulations describe the measured solvation dynamics. a, Measured difference scattering signal after subtracting the well-characterized $\Delta S^{\text{solvent-solvent}}(Q,t)$ contribution due to the temperature increase of bulk water. A three-point median filter along the time axis is applied to the data. **b**–**d**, Difference scattering signals calculated from non-equilibrium MD simulations and arising from changes in solute–solvent atom-pair distances. Five simulations with different t_{BET} were performed. As an example, panels **c** and **d** show the difference scattering signals calculated from non-equilibrium MD simulations with $t_{\text{BET}} = 60$ fs and $t_{\text{BET}} = 150$ fs, respectively. Panel **b** shows the final simulation obtained by a linear combination of the five simulations according to the MMCT state fraction and lifetime, obtained from the analysis of the Fe Kβ data. Calculated signals are convoluted with the instrument response function.

subtracted from the data as described in Supplementary Discussion 3 and it is not further considered here.

We focus our analysis on the difference scattering signal arising from changes in solute–solute and solute–solvent atom-pair distances. This is done by comparison of the XSS data with the scattering signals calculated from the solute–solute and solute–solvent radial distribution functions (RDFs) generated by MD simulations ($\Delta S_{\text{sim}}^{\text{solute-solute}}$ and $\Delta S_{\text{sim}}^{\text{solute-solvent}}$, respectively). In the MD simulations, we used the solute structure and electrostatic potential partial charges in the ground state (GS) and MMCT state calculated using explicit solvent time-dependent density functional theory (TDDFT). The structures were fixed and embedded in a water box, as described in the Methods.

Equilibrium MD simulations of the GS and MMCT state of FeRu were initially performed. Figure 4 shows the $\Delta S_{\text{sim}}^{\text{solute-solute}}$ (blue line) and $\Delta S_{\text{sim}}^{\text{solute-solvent}}$ (magenta line) signals obtained from the difference of the MMCT and GS scattering simulations. The main distinction between the TDDFT-calculated structures is a ~0.13 Å contraction of the Fe–Ru distance in the MMCT state with respect to the GS. This yields a small positive contribution in the low-Q region of the $\Delta S_{\text{sim}}^{\text{solute-solute}}$ signal, inconsistent with the measurements. Further intramolecular structural considerations were also unable to reproduce the experimental data, and are described in Supplementary Discussion 4. By contrast, $\Delta S_{\text{sim}}^{\text{solute-solvent}}$ shows a negative signal in the low-Q region, consistent with the measured data, reflecting the increased solute–solvent distances in the excited state compared to the ground state. The magnitude of $\Delta S_{\text{sim}}^{\text{solute-solvent}}$ is much larger than that of $\Delta S_{\text{sim}}^{\text{solute-solute}}$, indicating that the measured difference scattering signal at $Q < 1.5$ Å^{-1} is dominated by solvent reorganization.

There are two possible contributions to the solute–solvent interactions that dominate the scattering signal: (1) the response of the solvent to the changes in charge distribution (dielectric solvation), and (2) the response of the solvent to the changes in solute size (mechanical solvation). These contributions can be distinguished through additional equilibrium MD simulations, modelled after previous work[20,42]. Two distinct excited-state models of FeRu are constructed based on (1) the GS structure and the MMCT partial charges (purely dielectric), and (2) the MMCT structure and the GS partial charges (purely mechanical). Figure 4 shows the difference scattering traces obtained from these two models, making it clear that dielectric contributions dominate and mechanical ones can be neglected. Therefore, $\Delta S^{\text{solute-solvent}}$ is attributed to photoinduced changes in the electrostatic interaction between FeRu and water molecules. The simulated increase in solute–solvent distances is consistent with the expected weakening of hydrogen bonds in the excited state compared to the ground state, as discussed below.

To describe the solvation dynamics upon 800 nm excitation of FeRu in water, we performed non-equilibrium MD simulations[20,42–44]. We aim to reproduce and interpret the measured difference scattering signal after removal of the $\Delta S^{\text{solvent-solvent}}$ contribution, as shown in Fig. 5a. Based on the above discussion, intramolecular structural changes of FeRu do not contribute to the measured difference scattering signal shown in Fig. 5a and were therefore neglected in the simulations. The non-equilibrium simulations start from 1,000 configurations from the equilibrium MD simulation of FeRu in the GS. At $t = 0$, the partial charges of the solute are switched to the MMCT values, creating a non-equilibrium configuration, and the subsequent non-equilibrium dynamics are recorded every 10 fs. After a time delay of $t = t_{\text{BET}}$, the atomic charges of the solute are switched back to the GS values, mimicking BET. Five non-equilibrium simulations were run with $t_{\text{BET}} = 30$, 60, 90, 150 and 210 fs. Figure 5c,d shows the results obtained with $t_{\text{BET}} = 60$ and $t_{\text{BET}} = 150$ fs, respectively, while the other simulations are presented in Supplementary Fig. 12. Each simulation reproduces the main features observed in the measurements: the negative low-Q signal indicative of expansion of solute–solvent distances, and the positive feature at ~1.3 Å^{-1} that shifts with increasing time to lower Q values, yielding a time-dependent oscillation in the low-Q signal. The final simulated $\Delta S(Q,t)$ shown in Fig. 5b is then constructed as a linear combination of the five simulation results, weighted according to the exponential MMCT decay measured by Kβ XES (Supplementary Fig. 13). This non-equilibrium simulation qualitatively reproduces the measured features both in Q and time, and effectively captures the time-oscillatory feature observed in the low-Q part of the measured scattering signal, as shown in Fig. 3b. The analysis of the MD simulations reveals that collective water translational motions arising from a change in the hydrogen bond strength with FeRu are responsible for the key features of the data, as described in the next section.

Coherent translational motion of the first solvation shell coupled to BET. Analysis of the MD simulations reveals atomic-scale information about solvent reorganization. As detailed in Supplementary Discussion 6, the simulation shows a highly structured and oriented first solvation shell for the electronic ground state of FeRu. This results from hydrogen bonding between water and (1) the hydrogen-bond-accepting nitrogens of the cyano-ligands bound

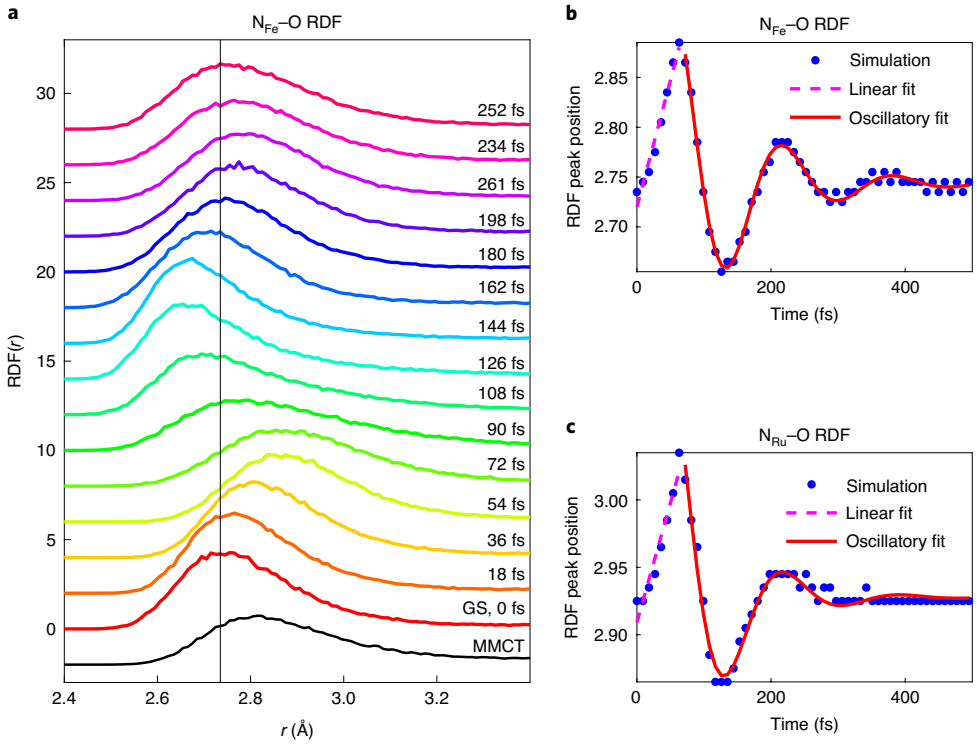

Fig. 6 | Results of non-equilibrium MD simulations. a, N_{Fe}–O RDF as a function of time, with MMCT excitation at $t = 0$ and $t_{BET} = 60$ fs. The black vertical line marks the position of the first-solvation-shell peak in the GS. The RDF of the equilibrated MMCT state is shown for reference (black RDF). **b**,**c**, Time evolution of the first-solvation-shell peak position for the N_{Fe}–O and N_{Ru}–O RDFs, respectively. The simulations can be described by a linear fit at early times, before BET (dashed purple line), and by a damped oscillator at later times, after BET (red line). In **b**, the first solvation shell surrounding the N_{Fe} atoms expands with an average velocity of 2.5 Å ps^{-1} upon MMCT. BET initiates contraction of the solvation shell, which oscillates with a period of 165 ± 2 fs and is damped in 104 ± 9 fs. In **c**, for the first solvation shells surrounding the N_{Ru} atoms, the velocity of the initial expansion is 1.8 Å ps^{-1}, followed by 174 ± 9 fs oscillations, which are damped in 77 ± 10 fs.

to Fe (N_{Fe}) and (2) the hydrogen-bond-donating nitrogens of the amine-ligands bound to Ru (N_{Ru}). We therefore illustrate the motions of the first solvent shell by the changes in the hydrogen-bonded atom-pair distances. Figure 6a shows the temporal evolution of the N_{Fe}–O RDF from the non-equilibrium MD simulation with $t_{BET} = 60$ fs. This RDF shifts to a higher distance (r) upon MMCT and reverses direction upon BET, overshooting the original position and undergoing a damped oscillation back to the GS position.

The oscillatory motion of the first solvation shell is clearly evident in Fig. 6b,c, which plots the distance (r) corresponding to the maximum of the N_{Fe}–O and N_{Ru}–O RDFs as a function of time. A linear fit for time delays <60 fs yields average expansion velocities of 2.5 Å ps^{-1} and 1.8 Å ps^{-1} of the first solvent shells around the Fe and Ru ligands respectively, upon MMCT. Maximum displacements of 0.15 Å (Fe) and 0.11 Å (Ru) are reached at $t = 60$ fs, where BET is initiated. Using a damped oscillator model to characterize the subsequent temporal evolution, we find that the oscillations of the N_{Fe}–O and N_{Ru}–O RDFs have a frequency of approximately 200 cm^{-1} and relaxation times of ~100 fs. In considering all the non-equilibrium simulations with varying t_{BET} (Supplementary Discussion 6), the oscillation frequency varies from 120 cm^{-1} to 200 cm^{-1}, with the smaller frequency corresponding to later BET, as expected from the anharmonicity of the solute–solvent interaction potential. The observed frequencies are in good agreement with the ~180 cm^{-1} peak present in the low-frequency vibrational spectrum of water and assigned to translational motions of the intermolecular hydrogen bonding coordinate[45].

Overall, analysis of the simulated RDFs indicates that (1) the low-Q difference scattering signal measured at the shortest time delays ($<t_{BET}$) arises from the coherent centre-of-mass translation of water molecules away from FeRu as hydrogen bonding is weakened due to the MMCT transition, and (2) the subsequent temporal oscillation in the low-Q difference scattering signal reflects the return of the solvation shell upon BET, as mediated by the intermolecular hydrogen bonding coordinate of water. These solvent translational motions can be described using a classical model that takes into account photoinduced changes in electrostatic interactions between the solute and solvent atoms. These are described in our MD simulations by using different sets of atomic partial charges for the GS and MMCT state of FeRu. An extended analysis (Supplementary Discussion 6) indicates that additional rotational and diffusional motions play a minor role in the structural reorganization of the first solvation shell on the MMCT and BET timescales.

Finally, a quantitative analysis of the solute–solvent interaction energy from the non-equilibrium MD simulations reveals that linear response theory fails to describe the BET process in FeRu (Supplementary Fig. 21). This observation is in agreement with earlier computational studies of mechanical solvation, where translational motions are found to lead to breakdown of linear response theory[43,44,46]. The energetic contributions of the water translational motions observed in our experiment to the overall solvent response upon electron transfer requires a full quantum-mechanical treatment of the solute–solvent interactions, as discussed in Supplementary Discussion 7.

Conclusions

We use FeRu as a prototype for studying the influence of the solvent in intramolecular electron-transfer reactions. The electron transfer between the Fe and Ru atoms in FeRu changes the oxidation state

of the metal centres and, as a consequence of different metal–ligand interactions, the electronic charge distribution on the ligand atoms. This leads to a change both in the molecular dipole moment (estimated to be 3.5 D from the calculated partial charges) and in the strengths of the hydrogen bond interactions between the ligands and the surrounding water molecules. Previous studies of dielectric solvation in water by traditional optical techniques, such as fluorescence Stokes shift experiments, have shown that dipolar solvation is dominated by long-range high-frequency motions (librations) of the water molecules[9]. These studies are, however, relatively insensitive to changes in the hydrogen bonding between the solute and the solvent[13,47,48]. Optical pump–probe spectroscopy studies could not directly identify the solvent modes promoting the electron transfer in FeRu and similar mixed-valence systems[28,30]. In this work, we have exploited the unique sensitivity of time-resolved XSS to changes in solute–solvent distances to capture the reorganization of the first solvation shell due to changes in the short-range solute–solvent electrostatic interactions upon MMCT excitation of FeRu. By analysing the time-resolved XSS signal in combination with the Fe Kβ XES data recorded simultaneously and with non-equilibrium MD simulations, we found that a large (tenths of ångströms) coherent (~180 cm^{-1}) translational motion of the water molecules hydrogen bonded to FeRu is coupled to the photoinduced MMCT and subsequent ultrafast (62 fs) BET. We therefore conclude that the observed coherent water translational motions contribute to the reorganization energy of the electron-transfer process in FeRu, as well as the water librations and the FeRu intramolecular vibrations previously considered[7,28,30]. Our work demonstrates the strong modification of solute–solvent hydrogen bonding induced by electronic excitation of the solute and addresses the long-standing question of how specific solute–solvent interactions respond to intramolecular electron transfer.

Translational solvent motions have also been proposed as important for controlling electron-transfer dynamics in non-aqueous solvents. For example, they are thought to be responsible for the electron detachment in charge transfer to solvent excitation of the sodium atom[21,42]. However, these motions were not directly observed. The ability to directly monitor the local translational motions, and to reveal the detailed nature of the first-solvation-shell interactions with the solute, paves the way for a mechanistic understanding of solvation processes coupled to charge-transfer reactions in solution, beyond the traditional description based on continuum solvent models and linear response. This will enable systematic and quantitative descriptions of how electron transfer is influenced by both solute and solvent molecular properties, to ultimately control and exploit such processes. Finally, specific hydrogen bonding interactions can play a critical role in biologically relevant chemical reactions, for example influencing the conformational changes critical to protein function[49,50]. Our method could thus be applied to understand how specific solute–solvent interactions influence a wider range of chemical reactions.

Online content

Any methods, additional references, Nature Research reporting summaries, source data, extended data, supplementary information, acknowledgements, peer review information; details of author contributions and competing interests; and statements of data and code availability are available at https://doi.org/10.1038/s41557-020-00629-3.

Received: 12 June 2020; Accepted: 14 December 2020;
Published online: 15 February 2021

References

1. Marcus, R. & Sutin, N. Electron transfers in chemistry and biology. *Biochim. Biophys. Acta* **811**, 265–322 (1985).
2. Rossky, P. J. & Simon, J. D. Dynamics of chemical processes in polar solvents. *Nature* **370**, 263–269 (1994).
3. Chen, P. & Meyer, T. J. Medium effects on charge transfer in metal complexes. *Chem. Rev.* **98**, 1439–1478 (1998).
4. Carpenter, B. K., Harvey, J. N. & Orr-Ewing, A. J. The study of reactive intermediates in condensed phases. *J. Am. Chem. Soc.* **138**, 4695–4705 (2016).
5. Kumpulainen, T., Lang, B., Rosspeintner, A. & Vauthey, E. Ultrafast elementary photochemical processes of organic molecules in liquid solution. *Chem. Rev.* **117**, 10826–10939 (2017).
6. Raineri, F. O. & Friedman, H. L. *Solvent Control of Electron Transfer Reactions* 81–189 (John Wiley & Sons, 2007).
7. Barbara, P. F., Walker, G. C. & Smith, T. P. Vibrational modes and the dynamic solvent effect in electron and proton transfer. *Science* **256**, 975–981 (1992).
8. Barbara, P. F., Meyer, T. J. & Ratner, M. A. Contemporary issues in electron transfer research. *J. Phys. Chem.* **100**, 13148–13168 (1996).
9. Jimenez, R., Fleming, G. R., Kumar, P. V. & Maroncelli, M. Femtosecond solvation dynamics of water. *Nature* **369**, 471–473 (1994).
10. Hsu, C.-P., Song, X. & Marcus, R. A. Time-dependent Stokes shift and its calculation from solvent dielectric dispersion data. *J. Phys. Chem. B* **101**, 2546–2551 (1997).
11. de Boeij, W. P., Pshenichnikov, M. S. & Wiersma, D. A. Ultrafast solvation dynamics explored by femtosecond photon echo spectroscopies. *Ann. Rev. Phys. Chem.* **49**, 99–123 (1998).
12. Underwood, D. F. & Blank, D. A. Ultrafast solvation dynamics: a view from the solvent's perspective using a novel resonant-pump, nonresonant-probe technique. *J. Phys. Chem. A* **107**, 956–961 (2003).
13. Petrone, A., Donati, G., Caruso, P. & Rega, N. Understanding THz and IR signals beneath time-resolved fluorescence from excited-state ab initio dynamics. *J. Am. Chem. Soc.* **136**, 14866–14874 (2014).
14. Błasiak, B., Londergan, C. H., Webb, L. J. & Cho, M. Vibrational probes: from small molecule solvatochromism theory and experiments to applications in complex systems. *Acc. Chem. Res.* **50**, 968–976 (2017).
15. Baiz, C. R. et al. Vibrational spectroscopic map, vibrational spectroscopy, and intermolecular interaction. *Chem. Rev.* **120**, 7152–7218 (2020).
16. Nibbering, E. T. J. & Elsaesser, T. Ultrafast vibrational dynamics of hydrogen bonds in the condensed phase. *Chem. Rev.* **104**, 1887–1914 (2004).
17. Bakker, H. J. & Skinner, J. L. Vibrational spectroscopy as a probe of structure and dynamics in liquid water. *Chem. Rev.* **110**, 1498–1517 (2010).
18. Kuharski, R. A. et al. Molecular model for aqueous ferrous–ferric electron transfer. *J. Chem. Phys.* **89**, 3248–3257 (1988).
19. Fonseca, T. & Ladanyi, B. M. Solvation dynamics in methanol: solute and perturbation dependence. *J. Mol. Liq.* **60**, 1–24 (1994).
20. Maroncelli, M. & Fleming, G. R. Computer simulation of the dynamics of aqueous solvation. *J. Chem. Phys.* **89**, 5044–5069 (1988).
21. Martini, I. B., Barthel, E. R. & Schwartz, B. J. Optical control of electrons during electron transfer. *Science* **293**, 462–465 (2001).
22. Kim, K. H. et al. Direct observation of bond formation in solution with femtosecond X-ray scattering. *Nature* **518**, 385–389 (2015).
23. Biasin, E. et al. Femtosecond X-ray scattering study of ultrafast photoinduced structural dynamics in solvated $[Co(terpy)_2]^{2+}$. *Phys. Rev. Lett.* **117**, 013002 (2016).
24. Haldrup, K. et al. Ultrafast X-ray scattering measurements of coherent structural dynamics on the ground-state potential energy surface of a diplatinum molecule. *Phys. Rev. Lett.* **122**, 063001 (2019).
25. Kunnus, K. et al. Vibrational wavepacket dynamics in Fe carbene photosensitizer determined with femtosecond X-ray emission and scattering. *Nat. Commun.* **11**, 634 (2020).
26. van Driel, T. B. et al. Atomistic characterization of the active-site solvation dynamics of a model photocatalyst. *Nat. Commun.* **7**, 13678 (2016).
27. Courtney, T. L., Fox, Z. W., Estergreen, L. & Khalil, M. Measuring coherently coupled intramolecular vibrational and charge-transfer dynamics with two-dimensional vibrational-electronic spectroscopy. *J. Phys. Chem. Lett.* **6**, 1286–1292 (2015).
28. Reid, P. J., Silva, C., Barbara, P. F., Karki, L. & Hupp, J. T. Electronic coherence, vibrational coherence, and solvent degrees of freedom in the femtosecond spectroscopy of mixed-valence metal dimers in H_2O and D_2O. *J. Phys. Chem.* **99**, 2609–2616 (1995).
29. Wang, C., Mohney, B. K., Akhremitchev, B. B. & Walker, G. C. Ultrafast infrared spectroscopy of vibrational states prepared by photoinduced electron transfer in $(CN)_5FeCNRu(NH_3)_5^-$. *J. Phys. Chem. A* **104**, 4314–4320 (2000).
30. Son, D. H., Kambhampati, P., Kee, T. W. & Barbara, P. F. Femtosecond multicolor pump–probe study of ultrafast electron transfer of $[(NH_3)_5Ru^{III}NCRu^{II}(CN)_5]^-$ in aqueous solution. *J. Phys. Chem. A* **106**, 4591–4597 (2002).
31. Timpson, C. J., Bignozzi, C. A., Sullivan, B. P., Kober, E. M. & Meyer, T. J. Influence of solvent on the spectroscopic properties of cyano complexes of ruthenium(II). *J. Phys. Chem.* **100**, 2915–2925 (1996).
32. Lay, P. A., McAlpine, N. S., Hupp, J. T., Weaver, M. J. & Sargeson, A. M. Solvent-dependent redox thermodynamics of metal amine complexes. Delineation of specific solvation effects. *Inorg. Chem.* **29**, 4322–4328 (1990).

33. Wang, C. et al. Solvent control of vibronic coupling upon intervalence charge transfer excitation of $(CN)_5FeCNRu(NH_3)_5^-$ as revealed by resonance Raman and near-infrared absorption spectroscopies. *J. Am. Chem. Soc.* **120**, 5848–5849 (1998).
34. Slenkamp, K. M. et al. Investigating vibrational anharmonic couplings in cyanide-bridged transition metal mixed valence complexes using two-dimensional infrared spectroscopy. *J. Chem. Phys.* **140**, 084505 (2014).
35. Curtis, J. C., Sullivan, B. P. & Meyer, T. J. Hydrogen-bonding-induced solvatochromism in the charge-transfer transitions of ruthenium(II) and ruthenium(III) ammine complexes. *Inorg. Chem.* **22**, 224–236 (1983).
36. Ross, M. et al. Comprehensive experimental and computational spectroscopic study of hexacyanoferrate complexes in water: from infrared to X-ray wavelengths. *J. Phys. Chem. B* **122**, 5075–5086 (2018).
37. Kjær, K. S. et al. Finding intersections between electronic excited state potential energy surfaces with simultaneous ultrafast X-ray scattering and spectroscopy. *Chem. Sci.* **10**, 5749–5760 (2019).
38. Glatzel, P. & Bergmann, U. High resolution 1s core hole X-ray spectroscopy in 3d transition metal complexes—electronic and structural information. *Coord. Chem. Rev.* **249**, 65–95 (2005).
39. Dohn, A. O. et al. On the calculation of X-ray scattering signals from pairwise radial distribution functions. *J. Phys. B* **48**, 244010 (2015).
40. Ihee, H. et al. Ultrafast X-ray diffraction of transient molecular structures in solution. *Science* **309**, 1223–1227 (2005).
41. Kjær, K. S. et al. Introducing a standard method for experimental determination of the solvent response in laser pump, X-ray probe time-resolved wide-angle X-ray scattering experiments on systems in solution. *Phys. Chem. Chem. Phys.* **15**, 15003–15016 (2013).
42. Barthel, E. R., Martini, I. B. & Schwartz, B. J. How does the solvent control electron transfer? Experimental and theoretical studies of the simplest charge transfer reaction. *J. Phys. Chem. B* **105**, 12230–12241 (2001).
43. Aherne, D., Tran, V. & Schwartz, B. J. Nonlinear, nonpolar solvation dynamics in water: the roles of electrostriction and solvent translation in the breakdown of linear response. *J. Phys. Chem. B* **104**, 5382–5394 (2000).
44. Fonseca, T. & Ladanyi, B. M. Breakdown of linear response for solvation dynamics in methanol. *J. Phys. Chem.* **95**, 2116–2119 (1991).
45. Castner, E. W., Chang, Y. J., Chu, Y. C. & Walrafen, G. E. The intermolecular dynamics of liquid water. *J. Chem. Phys.* **102**, 653–659 (1995).
46. Bragg, A. E., Cavanagh, M. C. & Schwartz, B. J. Linear response breakdown in solvation dynamics induced by atomic electron-transfer reactions. *Science* **321**, 1817–1822 (2008).
47. Chapman, C. F., Fee, R. S. & Maroncelli, M. Measurements of the solute dependence of solvation dynamics in 1-propanol: the role of specific hydrogen-bonding interactions. *J. Phys. Chem.* **99**, 4811–4819 (1995).
48. Sajadi, M., Weinberger, M., Wagenknecht, H.-A. & Ernsting, N. P. Polar solvation dynamics in water and methanol: search for molecularity. *Phys. Chem. Chem. Phys.* **13**, 17768–17774 (2011).
49. Bellissent-Funel, M.-C. et al. Water determines the structure and dynamics of proteins. *Chem. Rev.* **116**, 7673–7697 (2016).
50. Schirò, G. et al. Translational diffusion of hydration water correlates with functional motions in folded and intrinsically disordered proteins. *Nat. Commun.* **6**, 6490 (2015).

Methods

Data collection and reduction. The experiment was performed at the X-ray pump–probe instrument at the Linac Coherent Light Source XFEL. A 30 mM aqueous solution of FeRu was delivered through a nozzle producing a 50 µm circular liquid jet and recirculated, in a He environment. At $t = 0$, the sample was pumped with 4 µJ of 800 nm laser pulses of 45 fs (FWHM) duration and $100 \times 120\ \mu m^2$ spot size. After excitation, the sample was probed with 8 keV X-ray pulses (45 fs FWHM) at time delays ranging from −0.4 ps to 1.5 ps at a repetition rate of 120 Hz. The liquid jet pump speed was chosen so that fresh sample was hit for every pump–probe event. The time delay between the laser and the X-ray pulses was determined for every pump–probe event with ~10 fs (FWHM) resolution using the X-ray pump–probe timing tool[51].

Four cylindrically bent (0.5 m radius) Ge(620) crystal analysers were arranged in von Hamos geometry to diffract the Fe $3p1s$ $K\beta_{1,3}$ fluorescence from the sample onto a 140k Cornell-SLAC Pixel Array Detector[52], covering a Bragg angle from 78.2° to 80.6° and an energy range from 7.03 eV to 7.08 eV. The total ground state fluorescence spectra were corrected for background and common mode noise and scaled to the ground state spectra of ferrocyanide (as detailed in Supplementary Discussion 1). Reference Kβ fluorescence spectra of ferrocyanide ($[Fe(II)(CN)_6]^{4-}$) and ferricyanide ($[Fe(III)(CN)_6]^{3-}$) were measured at beamline 7-ID-D at the Advanced Photon Source using the same conditions and emission spectrometer described in ref. [36].

At the Linac Coherent Light Source, elastically scattered X-rays were collected on a 2.3M Cornell-SLAC Pixel Array Detector placed after the sample and perpendicular to the propagation direction of the X-ray beam, covering scattering vector Q up to 4.5 $Å^{-1}$. Two-dimensional scattering patterns were corrected for X-ray polarization and solid angle before extracting one-dimensional isotropic and anisotropic scattering signals, following a procedure previously published[53]. The analysis of the anisotropic part of the scattering signal is presented in Supplementary Discussion 8. The total scattering signals were scaled to the calculated scattering from a liquid unit cell (1 FeRu molecule and approximately 18,500 water molecules) yielding signals in electron units per solute molecule.

Difference signals for the XES and the XSS measurements were constructed by subtracting from the full datasets the signal measured from the unexcited sample. Difference signals were sorted according to the time delay measured by the timing tool, and averaged in approximately 30 fs time-bins. Difference scattering signals are of the order of 0.02% of the total scattering signal, which is dominated by the contribution from the bulk solvent (Supplementary Fig. 3).

Simulations. First, a quantum-mechanics/molecular-mechanics simulation of FeRu was performed in the ground state[36]. After equilibration, a cluster (238 atoms) was extracted comprising FeRu and water molecules contained in a 4 Å shell around the complex. Excited-state geometries of the solvated FeRu cluster were calculated by optimizing this snapshot on the MMCT potential energy surface using TDDFT[54]. For the analysis described in the main text, the GS geometry has the electron localized on Fe, whereas the MMCT excited-state geometry has the electron localized on Ru. The electrostatic potential partial atomic charges for the ground- and excited-state geometries were computed using the corresponding electron densities. The quantum-mechanics/molecular-mechanics and TDDFT calculations were performed with the PBE0 functional[55], and all calculations were performed with the NWChem computational chemistry program[56]. Both density functional theory and TDDFT offer the best compromise between accuracy and computational performance for the large explicitly solvated transition metal clusters considered in this study. We have successfully used the same approach in other studies leading up to this work. Further details are provided in Supplementary Discussion 9.

The resulting GS, MMCT excited-state geometries and corresponding electrostatic potential partial atomic charges are then used in classical MD simulations, where the solute structure is fixed in space and embedded in a cubic water box of 60 Å size. In the MD simulations, the intermolecular interactions are represented by site–site Lennard-Jones plus Coulombic potentials with parameters taken from the TIP4P-Ew force field potential[57] for water and OPLS2005 force field[58] for the solute. The MD simulations are carried out in canonical ensemble at an average temperature of 300 K. The simulations of the GS and MMCT state of FeRu are run for 4 ns. From the GS trajectory, equally spaced frames are extracted and used as a starting point for the non-equilibrium simulations described in the Results. RDFs of the atom-pair distances are obtained from the MD simulations and used to calculate isotropic scattering signals following the procedure in ref. [39]. The RDFs and corresponding scattering signals, as well as the experimental data, are available from ref. [59].

Data availability

The experimental data and the simulation results that support the findings of this study are available in Figshare with the identifier https://doi.org/10.6084/m9.figshare.13322975 (ref. [59]).

References

51. Minitti, M. P. et al. Optical laser systems at the Linac Coherent Light Source. *J. Synchrotron Radiat.* **22**, 526–531 (2015).
52. Philipp, H. T., Hromalik, M., Tate, M., Koerner, L. & Gruner, S. M. Pixel array detector for X-ray free electron laser experiments. *Nucl. Instrum. Methods Phys. Res. A* **649**, 67–69 (2011).
53. Biasin, E. et al. Anisotropy enhanced X-ray scattering from solvated transition metal complexes. *J. Synchrotron Radiat.* **25**, 306–315 (2018).
54. Silverstein, D. W., Govind, N., van Dam, H. J. & Jensen, L. Simulating one-photon absorption and resonance Raman scattering spectra using analytical excited state energy gradients within time-dependent density functional theory. *J. Chem. Theory Comput.* **9**, 5490–5503 (2013).
55. Adamo, C. & Barone, V. Toward reliable density functional methods without adjustable parameters: the PBE0 model. *J. Chem. Phys.* **110**, 6158–6170 (1999).
56. Aprà, E. et al. NWChem: past, present, and future. *J. Chem. Phys.* **152**, 184102 (2020).
57. Horn, H. W. et al. Development of an improved four-site water model for biomolecular simulations: TIP4P-Ew. *J. Chem. Phys.* **120**, 9665 (2004).
58. Jorgensen et al., W. L. Development and testing of the OPLS all-atom force field on conformational energetics and properties of organic liquids. *J. Am. Chem. Soc.* **118**, 11225–11236 (1996).
59. Biasin, E., Schoenlein, R. W., Govind, N. & Khalil, M. Time-resolved X-ray scattering and spectroscopy data and MD simulations reveal solvent motions coupled to intramolecular elecron transfer. *Figshare* https://doi.org/10.6084/m9.figshare.13322975 (2020).

Acknowledgements

This work was supported by the US Department of Energy, Office of Science, Office of Basic Energy Sciences, Chemical Sciences, Geosciences and Biosciences Division under award nos DE-SC0012450 (Z.W.F., J.M.C., J.D.G., Y.Z., S.M. and M.K.), DE-SC0019277 (C.L.-S. and M.K.), DE-FG02-04ER15571 (S.M.), KC-030105066418 (N.G.), KC-030105172685 (N.G.), DE-AC02-76SF00515 (E.B., K.L., K.S.K, K.H., J.H.L., M.R., K.J.G., R.W.S. and A.A.C) and DE-AC02-06CH11357 (G.D., A.M.M. and S.H.S.). J.D.G. acknowledges support by the National Science Foundation Graduate Research Fellowship Program (no. DGE-1256082). Use of the Linac Coherent Light Source, SLAC National Accelerator Laboratory, is supported by the US Department of Energy, Office of Science, Office of Basic Energy Sciences under contract no. DE-AC02-76SF00515. This research used resources of the Advanced Photon Source, a US Department of Energy Office of Science User Facility operated for the US Department of Energy Office of Science by Argonne National Laboratory under contract no. DE-AC02-06CH11357. This research benefited from computational resources provided by the Environmental Molecular Sciences Laboratory, a US Department of Energy Office of Science User Facility sponsored by the Office of Biological and Environmental Research and located at the Pacific Northwest National Laboratory. The Pacific Northwest National Laboratory is operated by Battelle Memorial Institute for the US Department of Energy under US Department of Energy contract no. DE-AC05-76RL1830. This research also used resources from the National Energy Research Scientific Computing Center, a US Department of Energy Office of Science User Facility operated under contract no. DE-AC02-05CH11231.

Author contributions

Z.W.F., K.S.K., R.A.-M., M.C., J.D.G., J.M.G., K.H., T.K., J.H.L., M.R., D.S., R.W.S., N.G., A.A.C. and M.K. prepared and conducted the experiment at the Linac Coherent Light Source. Z.W.F., K.H., J.H.L., G.D., A.M.M., S.H.S. and A.A.C. measured the reference iron spectra at the Advanced Photon Source. J.M.C. synthesized the sample. E.B. analysed the experimental data and performed the MD simulations. E.B and K.L. analysed the results from the MD simulations. A.A., Y.Z., S.M. and N.G. performed the quantum-mechanics/molecular-mechanics, density functional theory and TDDFT calculations. E.B., K.L., C.L.-S., K.J.G., R.W.S., N.G., A.A.C. and M.K. interpreted the results. E.B. and A.A.C. wrote the article with contributions from all authors.

Competing interests

The authors declare no competing interests.

Additional information

Supplementary information is available for this paper at https://doi.org/10.1038/s41557-020-00629-3.

Correspondence and requests for materials should be addressed to E.B., N.G., A.A.C. or M.K.

Peer review information *Nature Chemistry* thanks Mark Maroncelli, Simone Techert and the other, anonymous, reviewer(s) for their contribution to the peer review of this work.

Reprints and permissions information is available at www.nature.com/reprints.

nature portfolio

https://doi.org/10.1038/s41557-020-00629-3

Supplementary information

Direct observation of coherent femtosecond solvent reorganization coupled to intramolecular electron transfer

In the format provided by the authors and unedited

Supplementary Information: Direct observation of coherent femtosecond solvent reorganization coupled to intramolecular electron transfer

Elisa Biasin[1*], Zachary W. Fox[2], Amity Andersen[3], Kathryn Ledbetter[1], Kasper S. Kjær[1,4], Roberto Alonso-Mori[5], Julia M. Carlstad[2,12], Matthieu Chollet[5], James D. Gaynor[2,12], James M. Glownia[5], Kiryong Hong[6,10], Thomas Kroll[5], Jae Hyuk Lee[6,11], Chelsea Liekhus-Schmaltz[2], Marco Reinhard[1], Dimosthenis Sokaras[5], Yu Zhang[8,13], Gilles Doumy[7], Anne Marie March[7], Stephen H. Southworth[7], Shaul Mukamel[8], Kelly J. Gaffney[1], Robert W. Schoenlein[1,5], Niranjan Govind[9*], Amy A. Cordones[1*], and Munira Khalil[2*]

[1]Stanford PULSE Institute, SLAC National Accelerator Laboratory, Menlo Park, CA 94025, USA.
[2]Department of Chemistry, University of Washington, Seattle, Washington 98195, USA
[3]Environmental Molecular Sciences Division, Earth and Biological Sciences Directorate, Pacific Northwest National Laboratory, Richland, WA 99354, USA
[4]Technical University of Denmark, Department of Physics, Fysikvej 307, DK-2800 Kongens Lyngby, Denmark.
[5]LCLS, SLAC National Accelerator Laboratory, Menlo Park, CA 94025, USA.
[6]Ultrafast X-ray Science Laboratory, Chemical Sciences Division, Lawrence Berkeley National Laboratory, Berkeley, CA 94820, USA
[7]Chemical Sciences and Engineering Division, Argonne National Laboratory, Lemont, IL, 60439, USA
[8]Department of Chemistry, Physics, and Astronomy, University of California, Irvine, CA 92697, USA
[9]Physical Sciences Division, Physical and Computational Sciences Directorate, Pacific Northwest National Laboratory, Richland, WA 99354, USA

[10]Present Address: Gas Metrology Group, Division of Chemical and Biological Metrology, Korea Research Institute of Standards and Science, Daejeon, 34113, Republic of Korea
[11]Present Address: Pohang Accelerator Laboratory, Pohang, 37673, Republic of Korea
[12]Present Address: Department of Chemistry, University of California, Berkeley, CA 94720, USA
[13]Present Address: Q-Chem Inc., 6601 Owens Dr, Pleasanton, CA 94588, USA

Contents

1 Data Collection and Reduction

1.1 Sample

FeRu was prepared as its sodium salt (NaFeRu) according to literature methods and purified using a BioGel P2 column to remove starting material from sample [1]. Supplementary Fig. 1 shows the UV-Vis absorption spectrum of FeRu in water.

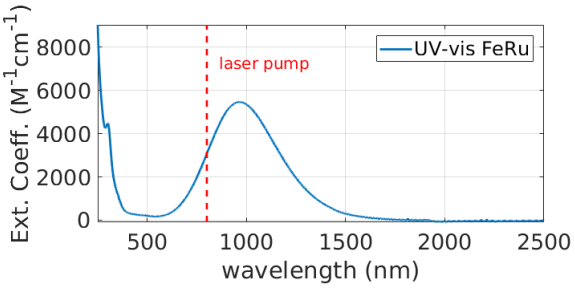

Supplementary Figure 1. UV-Vis spectrum of FeRu in water. The metal-to-metal charge-transfer band is centered at 955 nm and it's excited on the red side (800 nm).

1.2 Fe K$\beta_{1,3}$ XES

As described in the main text, an energy-dispersive X-ray spectrometer based on von Hamos geometry in combination with a 2D CSPAD was used to detect the Fe K$\beta_{1,3}$ fluorescence in a 7030-7080 eV energy range. With respect to a single-shot 2D image: a background due to dark current is subtracted for each pixel; a common mode correction is applied by shifting the zero photon peak (of the histograms of all-pixels measured intensity) at zero analogue-to-digital (ADU) units; a one-dimensional spectrum is constructed by averaging the measured intensity in the non-dispersive direction, disregarding the zero-photon peak by considering only intensity bigger than 20 ADU. Each 1D spectrum is self-normalized to the total integrated intensity. A global scaling factor is found by comparison of the ground state spectrum of FeRu to a reference (3p-1s)Kβ spectrum of $[Fe(II)(CN)_6]^{4-}$ (see Supplementary Fig. 2) and applied to the full dataset. Difference spectra are constructed by subtracting from all the spectra the average of the spectra measured without exciting the sample. 1000 difference spectra are averaged according to their time stamp, yielding time bins of approximately 30 fs width.

1.3 XSS signal

The X-ray scattering patterns were recorded on the CSPAD detector placed ∼6 cm after the sample. After subtracting a dark background and masking shadowed pixels, each measured scattering pattern was corrected for X-ray polarization and solid angle coverage. Common mode fluctuations were corrected by subtracting, for each tile, the average intensity measured on the unbonded pixels of that tile (pixels not exposed to photons). Sample-detector distance was calibrated by comparing the radially

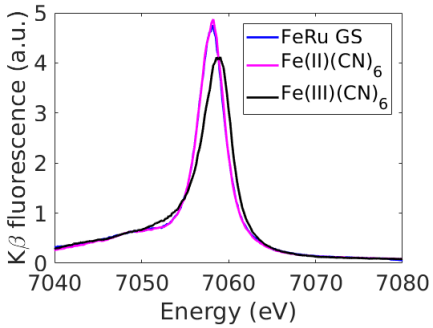

Supplementary Figure 2. Kβ fluorescence of ground state FeRu (blue line); Kβ fluorescence of $[Fe(II)(CN)_6]^{4-}$ (magenta line); Kβ fluorescence of $[Fe(III)(CN)_6]^{3-}$ (black line). The difference between the black and the magenta spectra yields the model difference spectra $\Delta K\beta^{model}$ in Equation 1.

integrated total scattering signal to a reference measurement of neat water [2]. This reference measurement was also used to scale (in the Q range 0.5-4 $Å^{-1}$) the measured signal to the scattering signal arising from a liquid unit cell, yielding the measured signal in electron units per solute molecule (e.u./molec.). For every fifth shot the scattering pattern of the sample was recorded without pump (laser-off scattering patterns). Difference scattering patterns were constructed by subtracting the average of the two nearest laser-off scattering patterns from each scattering pattern measured after pumping the sample. The difference scattering patterns were azimuthally integrated into 15 slices, from which the isotropic and anisotropic difference scattering signals were extracted [3]. Finally, the difference scattering patterns were time sorted into time bins of $\sim$ 30 fs width, each containing 50000 curves. Supplementary Fig. 3 shows the isotropic total and difference scattering signals for comparison.

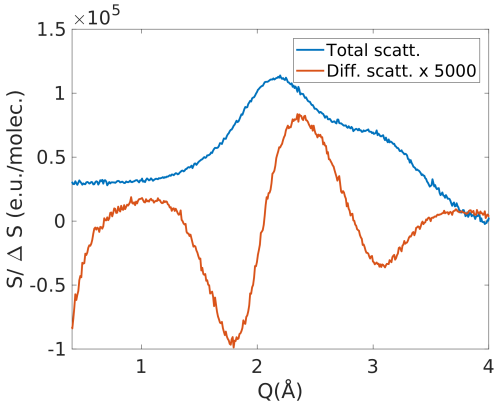

Supplementary Figure 3. Isotropic total and difference scattering signals. The total scattering (blue) shows the characteristic liquid peak from water. The difference scattering signal (orange), obtained by averaging the signals measured in the first 100 fs after 800 nm excitation of FeRu in water, is multiplied by 5000.

2 Excited-state population analysis

Supplementary Fig. 4 shows the results of a Singular Value Decomposition (SVD) of the transient Kβ data. As indicated by the relative magnitude of the singular values shown in Supplementary Fig. 4a, a single component dominates the signal. Supplementary Fig. 4b shows the energy-profile of the first component, overlaid by the scaled reference signal, constructed as the difference between the ground state Kβ spectra of $[Fe(III)(CN)_6]^{3-}$ and $[Fe(II)(CN)_6]^{4-}$ ($\Delta K\beta^{model}$).

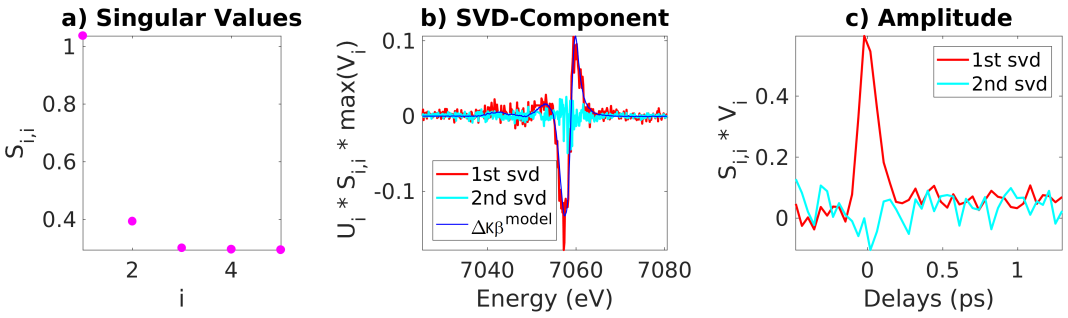

Supplementary Figure 4. SVD analysis of the XES transient data. $\Delta K\beta = U \cdot S \cdot V^{-1}$. a) The singular values of the diagonal $S_{i,i}$. b) Energy-profile of the components component ($U_i \cdot S_{i,i} \cdot \max(V_i)$). Only the first two components are shown for clarity. The first component is overlaid with $\Delta K\beta^{model}$. c) Temporal evolution of the component ($S_{i,i} \cdot V_i$).

The full Kβ dataset is described as:

$$\Delta K\beta(\epsilon, t) = \alpha(t)\Delta K\beta^{model}(\epsilon) \tag{1}$$

where α, the only fit parameter, represents the excited state fraction at each time delay. Supplementary Fig. 5 shows the comparison between the data (left panel), the model constructed by fitting Supplementary Eq. 1 to the data (middle panel), and the difference between the data and the model (right panel).

Fig. 2b in the main text shows the time-evolution of α obtained by fitting Supplementary Eq. 1 to the full dataset. The time-evolution of α is described by an exponential decay starting at the arrival time of the laser pump (t_0). An offset (c) is added to describe the incomplete recovery of the ground state. The time resolution of the experiment is included by convolution with the (Gaussian) Instrument Response Function (IRF) to yield the following expression for $\alpha(t)$:

$$\alpha(t) = \mathrm{IRF}(\sigma_{\mathrm{IRF}}, t) \otimes H(t - t_0)[Ae^{-\frac{t-t_0}{\tau}} + c] \tag{2}$$

where σ_{IRF} is the width of the IRF, A and τ are the amplitude and the lifetime of the exponential function representing, respectively, the initial excitation fraction and the lifetime of the MMCT state, and H is the Heaviside step function centered at t_0. The best-fit results obtained when fitting Supplementary Eq. 2 to the data are the following: $t_0 = 4 \pm 6$ fs; σ_{IRF}=35 ± 11 fs; A = 25 ± 4 %; τ=62 ± 10 fs; c = 0.01 ± 0.002. The fit is performed through a standard χ^2 minimization and the uncertainties are 95 % confidence bounds. For further discussion on the the long-lived photoproduct, see section 4.1.

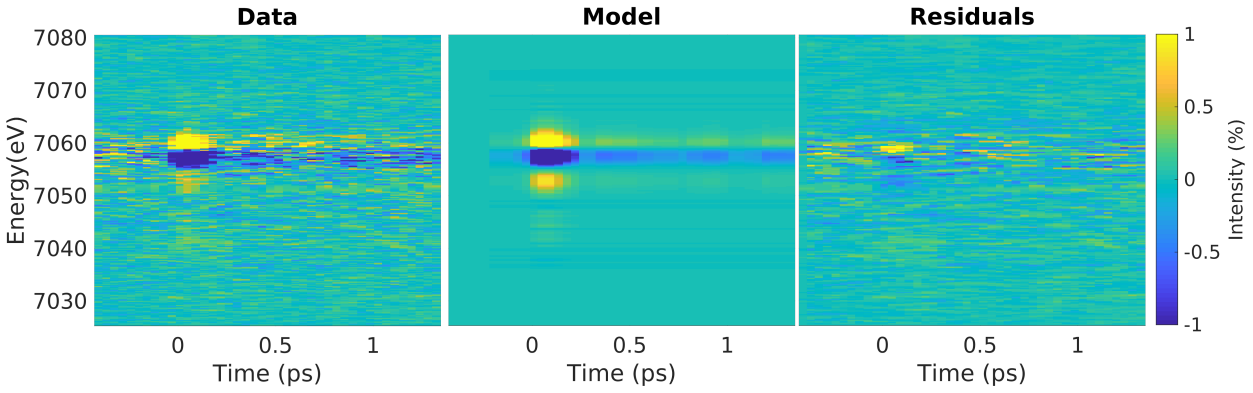

Supplementary Figure 5. (left) Difference transient Kβ spectra measured after photoexciting FeRu at 800 nm. (center) Model constructed by fitting Supplementary Eq. 1 to the measured data. (right) Difference between the measured data and the model. Units are in percentage with respect to the full Kβ fluorescence.

3 Bulk solvent contribution in the isotropic XSS dataset

The difference scattering signal arises from changes in solute–solute, solute–solvent, and solvent–solvent atom pair distances in the sample caused by the photoexcitation. For the isotropic signal, the solvent–solvent contribution arises mainly from the changes in bulk solvent caused by the non-radiative relaxation of the solute. At the time-scale explored in our measurement ($<$ 100 ps, before thermal expansion), the main contribution arises from the increase in temperature of water and the resulting difference scattering signal can be described as [2]:

$$\Delta \mathrm{S}^{\mathrm{solvent-solvent}}(\mathrm{Q,t}) = \Delta \mathrm{T(t)} \frac{\partial \mathrm{S(Q)}}{\partial \mathrm{T}}\bigg|_{\rho} \tag{3}$$

where $\frac{\partial \mathrm{S(Q)}}{\partial \mathrm{T}}\Big|_{\rho}$ describes a change in temperature at constant density, and ΔT the increase in temperature. The temperature solvent differential can be measured in separate experiments following published procedure and is well-characterized [2]. We find that the data for time-delay $>$ 0.5 ps, when the solute has relaxed to the ground state, is well-described by the model in Supplementary Eq. 3, as shown in Supplementary Fig. 6(left). For illustrative purposes, we fit Supplementary Eq. 3 to the entire dataset and use the fit results to subtract the temperature contribution from the measured dataset (Supplementary Fig. 7). This subtraction doesn't affect the region below Q $<$ 1.5 Å^{-1}, where the solute–solute and solute–solvent contributions dominate the difference scattering signal.

Supplementary Fig. 6(right) shows the best fit results obtained for ΔT after fitting Supplementary Eq. 3 to the entire dataset. The result shows an immediate increase of temperature following photoexcitation as observed and discussed in previous ultrafast studies [4]. At the longest time delay measured for this experiment (1.5 ps), the temperature of the bulk solvent has increased by approximately 0.2 K. The obtained value

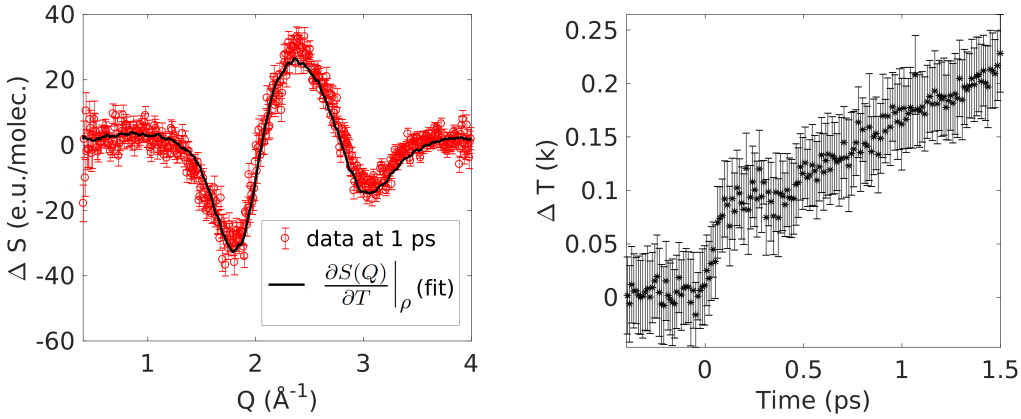

Supplementary Figure 6. (left) Difference scattering signal measured 1 ps after photoexcitation of FeRu. The signal is described by the characteristic scattering signal arising from an increase in temperature of water ($\frac{\partial S(Q)}{\partial T}\Big|_\rho$ in Supplementary Eq. 3). (right) Best fit results for ΔT after fitting Supplementary Eq. 3 to the entire dataset.

is in agreement with the increase in temperature expected following deposition of one 800 nm absorbed photon per excited molecule, as shown by the following calculations. Given an excitation fraction of 25 %, as found in our analysis, and considering the experimental parameters presented above, the number of excited molecules in the probed volume is approximately $7{\cdot}10^{13}$ molecules. At 1.5 ps, 99 % of the excited molecules have relaxed to the ground state, releasing 1.55 eV (800 nm) to the surrounding solvent molecules, which yield a total energy per unit volume of approximately 1.1 J/cm^3. Considering the specific heat capacity of water, and the average temperature change in the volume probed by the X-ray, the expected increase in temperature would then be approximately 0.26 K.

4 Intra-molecular structural changes considerations

From the analysis of the equilibrium MD simulations of the GS and MMCT state of FeRu, we observe that $\Delta S^{\text{solute–solute}}$ is negligible (as expected, due to rapid BET) with respect to $\Delta S^{\text{solute–solvent}}$ and that mechanical solvation plays a minor role compared to dielectric solvation (Fig. 4). Therefore, we conclude that intra-molecular structural changes can be neglected. Despite this, in this Discussion we explicitly exclude that the oscillatory feature in the low-Q part of the scattering signal could arise from intra-molecular vibrations or from possible structural changes involving the minor excitation channel (1 % offset in Fig. 2b).

Starting from possible vibrational effects, Supplementary Fig. 8 shows that the time evolution of the difference scattering signal averaged in the region Q=0.5 ± 0.1 Å^{-1} can be fit with a damped oscillator with a period of 0.39 ± 0.03 ps and lifetime of approximately 130 fs. Based on a normal mode analysis of the QM/MM calculation of FeRu in the GS state, no intra-molecular modes can be assigned to such period.

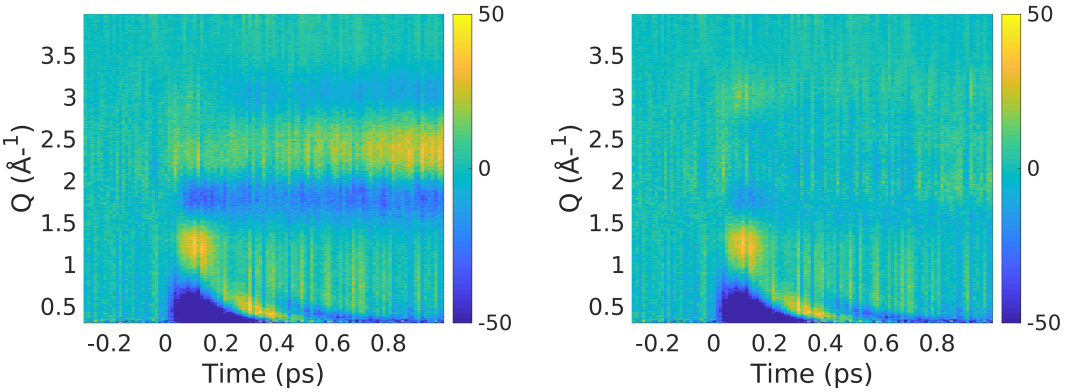

Supplementary Figure 7. (left) Difference scattering signal measured upon photoexcitation of FeRu in water at 800 nm. (right) Same dataset after subtraction of the component arising from an increase of the temperature of the bulk water, obtained by fitting Supplementary Eq. 3 to the entire dataset. The colorbar is saturated on the negative signals.

Specifically, the Fe-Ru stretching mode has the longest period ($\sim$ 220 fs) among the calculated intra-molecular modes. This value is consistent with the 210 fs period reported for the vibrational mode of the bond connecting two metal centers in a similar mixed-valence complex ($[(NH_3)_5Ru^{III}NCRu^{II}(CN)_5]^-$, RuRu) in aqueous solution [5]. Based on previous studies [4, 6, 7], if coherent Fe-Ru bond length oscillations would be the main photoinduced structural change in the sample, this would give rise to an oscillatory low-Q scattering signal with a period of 220 fs, which is not observed in our XSS data.

We have also excluded that the oscillatory feature in the low-Q part of the scattering signal could be related to the long-lived photoproduct by (1) analysing a dataset measured at a higher laser power with respect to the data described in main text, and (2) directly considering the scattering signal that could arise from, for instance, ionization or molecular damage. The analysis of point (1) is presented in section 4.1. Briefly, we show that the low-Q features of the scattering data scales approximately linearly with the MMCT excitation fraction, and not with the fraction of long-lived photoproduct. The analysis of point (2) is presented in the following. When irradiating aqueous $[Fe(CN)_6]^{4-}$ with UV–visible light, the two most likely photochemical processes are photooxidation, from population of a charge-transfer-to-solvent state, and photoaquation, which follows CN ligand dissociation [8]. Since structural changes between $[Fe(II)(CN)_6]^{4-}$ and $[Fe(III)(CN)_6]^{3-}$ are minimal [9], we consider instead potential CN ligand dissociation. Specifically, we consider the difference scattering signal arising from a) dissociation of the CN bridge, which leads to breaking of the FeRu molecule, b) dissociation of the equatorial ligands, c) dissociation of the axial CN ligand. Supplementary Fig. 9 shows the results obtained by using FeRu geometries modified in order to reflect the changes above. The positive peak observed in the data, which shows up at $\sim$ 1.3 Å^{-1} upon photoexcitation and shifts to Q $<$ 0.4 Å^{-1} with increasing time delay, is not reproduced by any of these simulations.

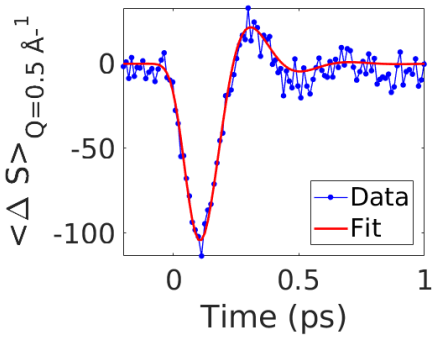

Supplementary Figure 8. Average scattering signal measured in the range $0.4 < Q < 0.6$ Å as a function of time-delay. The signal (blue points) is fit with a IRF-broaden damped oscillator with period of 0.39 ± 0.03 ps and a relaxation time of 0.13 ± 0.02 ps.

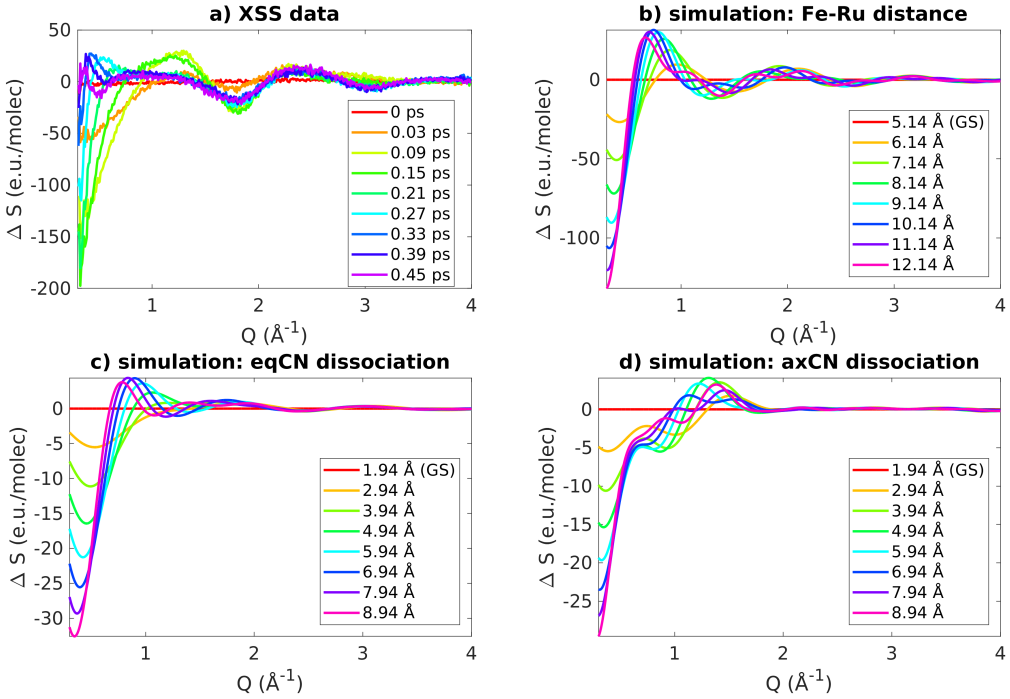

Supplementary Figure 9. a) Experimental ΔS as a function of time. b-c-d) Calculated $\Delta S^{\text{solute–solute}}$ arising from possible CN ligands dissociation. b) $\Delta S^{\text{solute–solute}}$ as a function of increasing Fe-Ru bond length distance, mimicking dissociation of the molecule at the CN bridge. c) $\Delta S^{\text{solute–solute}}$ as a function of increasing distance between one equatorial CN ligand and the Fe. d) $\Delta S^{\text{solute–solute}}$ as a function of increasing distance between the axial CN ligand and the Fe.

4.1 Comparison with a high laser power dataset

In this section, we present the analysis of a dataset recorded with a laser power of 50 μJ (417 mJ/cm^2) , compared to 4 μJ (33 mJ/cm^2), that was used for the main

dataset, while the other experimental parameters are left unchanged. The collection and reduction of the data was done following the procedure used for the low laser power data described above. From the comparison of the analysis between the low and high laser power data, presented below, we confirm that the low-Q oscillatory feature cannot be assigned to possible structural changes of the long-lived photoproduct (1 % offset in Fig. 2b).

Supplementary Fig. 10 (left) shows the Kβ transient data measured upon 800 nm photoexcitation of FeRu in water using a 50 μJ laser pulse. Supplementary Eq. 1 is used to to model this dataset. Supplementary Fig. 10 (center) shows an example of the fit at 50 fs, while Supplementary Fig. 10 (right) shows the best fit results for the free parameter α obtained from fitting the model in Supplementary Eq. 1 to the data. The fit is an exponential decay plus offset, as in Supplementary Eq. 2. The IRF and t_0 are kept fixed to the value obtained from the fit of the low laser power dataset, while the initial excitation fraction is found 34 ± 6 % (as opposed to 25 ± 4 % from the low-laser power data), the lifetime 0.21 ± 0.06 ps (as opposed to 62 ± 10 fs), and the offset 0.13 ± 0.01 (as opposed to 0.01 ± 0.002). These parameters are discussed in the following.

First, an excitation of ∼34 % is found because of the photoselection. Since the laser is linearly polarized and the transition dipole moment is parallel to the Fe-Ru axis, no more than 1/3 of the randomly oriented molecules can be excited to the MMCT state. Secondly, the fraction of long-lived photoproduct increases linearly with laser power, indicating that the long-lived species is due to a second linear absorption process. We propose that it could be a second single-photon excitation of the ground state with a low cross-section or excited state absorption of the MMCT state within the laser pulse envelope. Re-excitation after BET within the same pulse envelope also partially explain the longer BET time observed in the high laser power dataset. Barbara and coworker also observed a long-lived photoproduct, that they assigned to "spin-orbit excited state" [10]. Based on the shape of the long-lived Kβ signal, we conclude that the long-lived species is either a Fe(III) or a triplet MC state of the Fe [11]. However, the precise nature of the second linear excitation process cannot be established based on the available studies and it's outside of the scope of this work.

Supplementary Fig. 11(left) shows the difference scattering signal measured upon 800 nm photoexcitation of FeRu in water using a 50 μJ laser pulse. Supplementary Fig. 11(right) shows a comparison of the time-evolution of the difference scattering signal measured at two different Q values both at high and low laser power. The magnitude of the signals at these Q values scale roughly with the MMCT excitation fraction (a factor of 1.5) and does not scale with the signal corresponding to the long-lived photoproduct (a factor of 13). In conclusion, the low-Q scattering features upon which we have based the interpretation of the data arise only from dynamics related to the MMCT excitation.

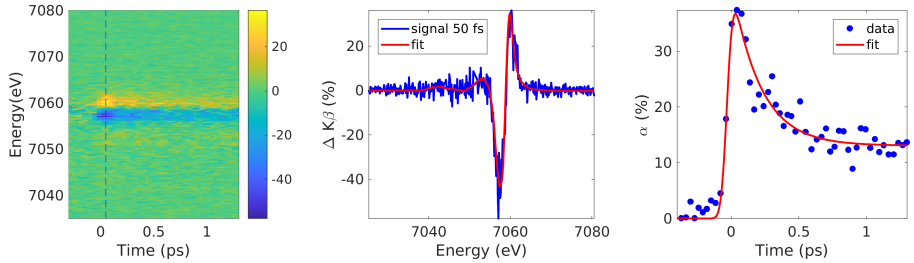

Supplementary Figure 10. Kβ Fe XES measured at high laser power. (left) Energy- and time-resolved ΔKβ data measured upon photoexcitation of FeRu in water with a 50 μJ laser pulse. b) Kβ transient measured at 50 fs. The red line shows the model signal ($\Delta K\beta^{model}$), calculated as the measured difference between the Kβ fluorescence of Fe(III)- and Fe(II)- hexacyanide. (right) Best-fit results obtained for α (the MMCT excitation fraction) by fitting Supplementary Eq. 1 to the measured ΔKβ spectra at each time delay. The red line is a fit of a IRF-broadened exponential decay plus offset.

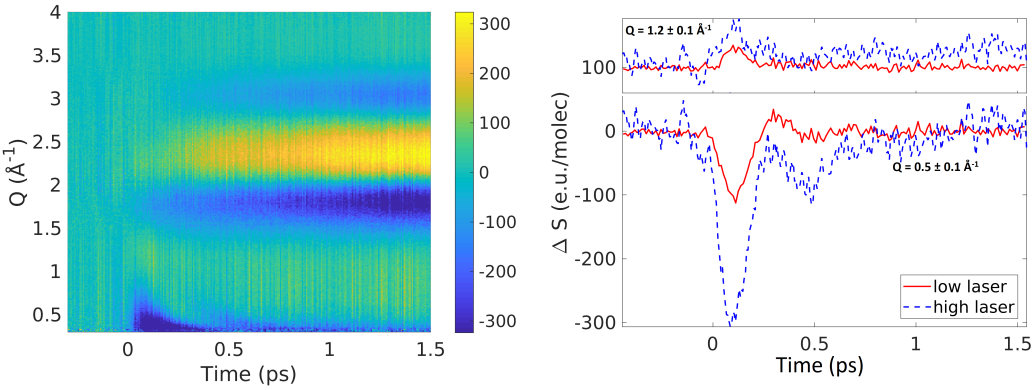

Supplementary Figure 11. Comparison of XSS signals measured at different laser power. (left) ΔS measured upon photoexcitation of FeRu in water with a 50 μJ laser pulse, as a function of scattering vector and time delay. (right) Comparison between the averaged difference scattering signal at Q=0.5±0.1 Å^{-1} and Q=1.2±0.1 Å^{-1} as a function of pump-probe time delay and of two different laser power.

5 Difference scattering signals calculated from non-equilibrium simulations

Supplementary Fig. 12 shows the difference scattering signal calculated from the solute–solvent Radial Distribution Functions (RDFs) obtained from the non-equilibrium simulations as a function of different BET times (t_{BET}). We note that each simulation shows the main features observed in the measured data: the negative low-Q signal indicative of expansion of solute–solvent distances, and the positive feature at $\sim$ 1.3 Å^{-1} that shifts to lower Q values as a function of time, yielding time-dependent oscillations in the low-Q signal. Fig. 5b in the main text is a linear combination of the five simulations, with linear coefficients corresponding to the fraction of excited state molecules

that have relaxed back to the GS at that specific t_{BET}. The linear coefficients are reported in Supplementary Fig. 13 and Supplementary Table 1. The simulated scattering signals are convoluted with the IRF.

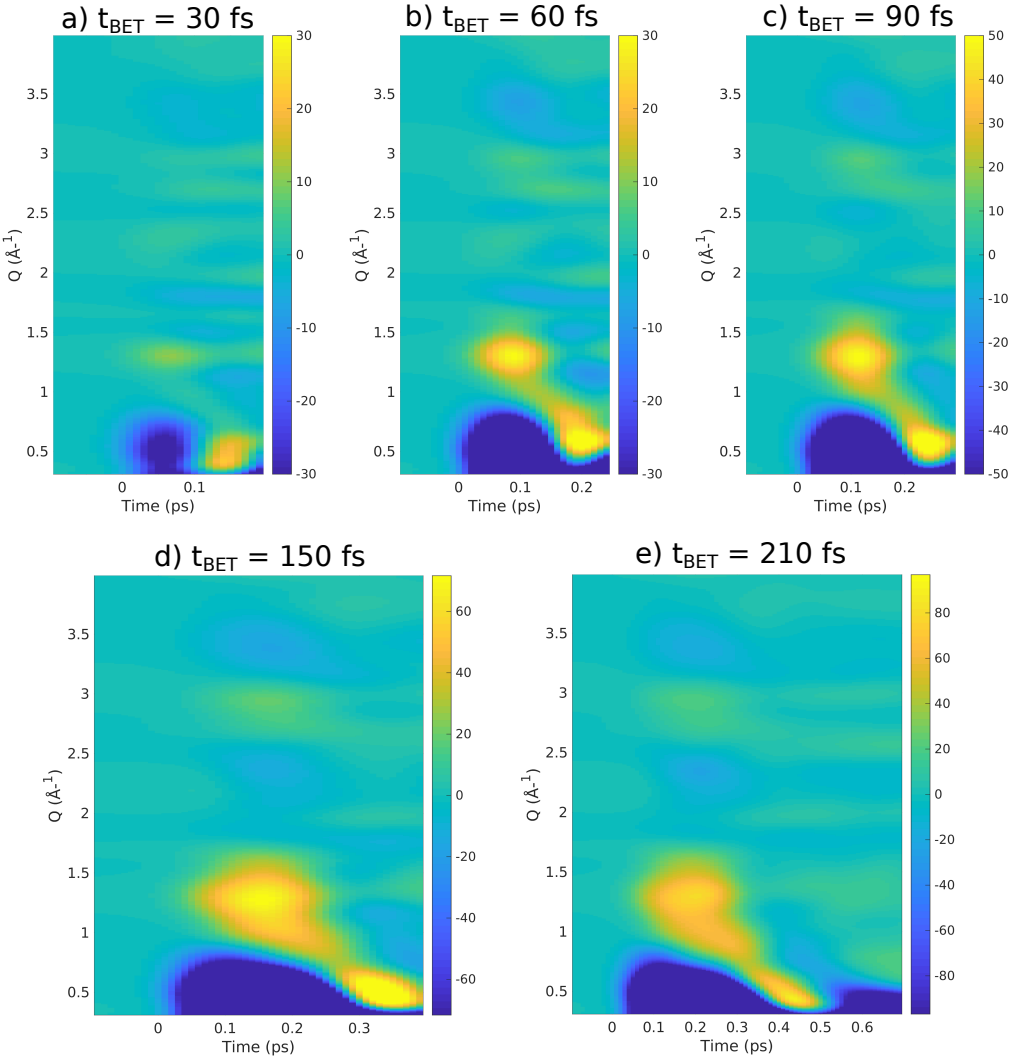

Supplementary Figure 12. Difference scattering signals calculated from the non-equilibrium MD simulations of FeRu in a water box, as a function of BET time. At t=0 the excited state partial charges are used for the solute. Starting from the upper left plot, the charges are switched back to the ground state values at 30 fs, 60 fs, 90 fs, 150 fs, and 210 fs respectively. Colorbar is saturated on the negative side. Signals are convoluted with the IRF.

5.1 Contributions of different solute–solvent atom pairs to the difference scattering signal

Supplementary Fig. 14 shows the contributions of the different solute–solvent atom pairs to the difference scattering signal calculated from the non-equilibrium simulations

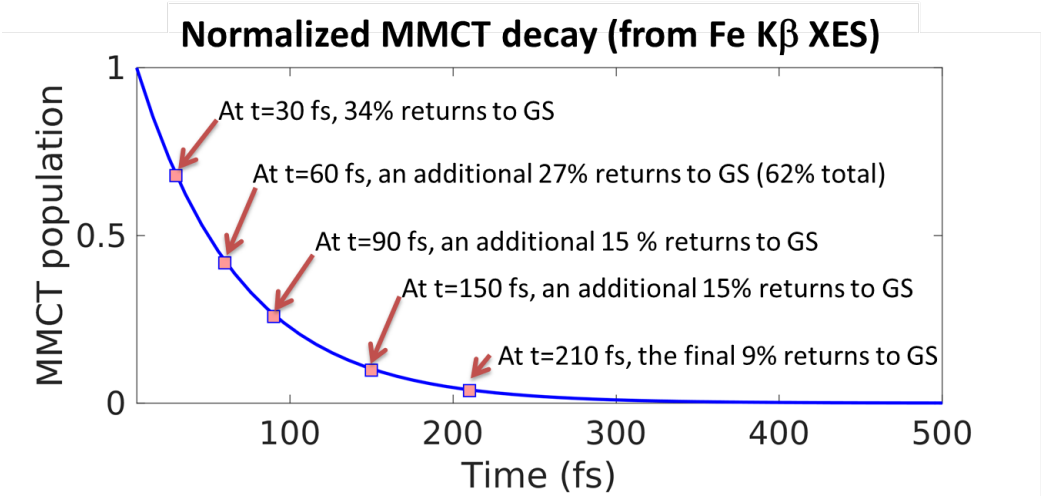

Supplementary Figure 13. Illustration of the weighting method used in the linear combination of the non-equilibrium simulation results with varied t_{BET} values. The exponential decay (62 fs lifetime) of the MMCT state measured via Fe Kβ XES (blue line) is used to identify the fractional population that has returned to the GS at each t_{BET} value. Accordingly, the weighting factors are 0.34 for t_{BET} = 30 fs, 0.27 for t_{BET} = 60 fs, 0.15 for t_{BET} = 90 fs, 0.15 for t_{BET} = 150 fs, 0.09 for t_{BET} = 210 fs.

at a specific time point. The larger contributions are expected from the pairs containing the most electron-rich atoms, considering also the number of atoms of the same type in the FeRu molecule. For instance, in terms of number of electrons, the contribution of the 11 nitrogens is nominally equivalent to the summed contribution of 1 Fe and 1 Ru atom. We also note that, since the solute structure is frozen during the MD simulations, the solute–solvent dynamics is independent of the solute–solvent RDF chosen to illustrate the dynamics.

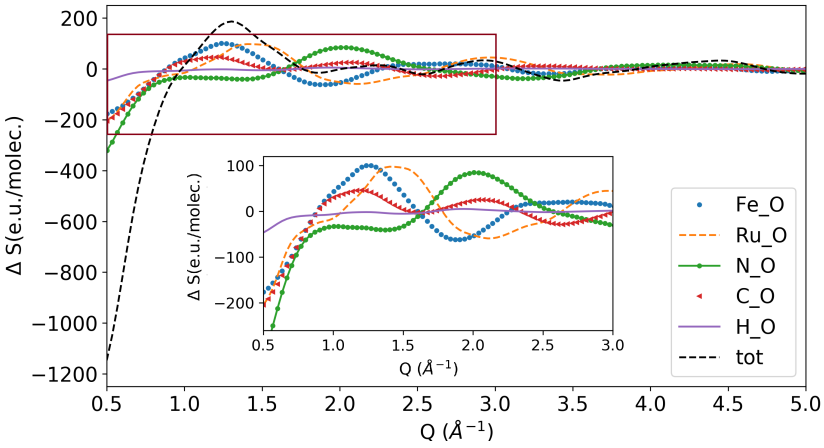

Supplementary Figure 14. Difference scattering signal calculated from the non-equilibrium MD simulations at a specific time-delay (60 fs) after the starting point of the simulation (when the partial charges are switched to the MMCT values). The dashed black line is the sum of the individual atom pairs contributions.

6 Extended analysis of the changes in the first solvation shell structure from MD simulations

6.1 Hydrogen bonding and GS Solvation Shell Structure

In order to visualize the structure of the solvation shell around the FeRu molecule, we calculate Spatial Distribution Functions (SDFs) from the MD simulations (see section 9.4). SDFs describe the 3D atomic density distribution as a function of two variables: the distance between pair of atoms (r) and the angle from a given axis (θ). In the following, we examine solute–solvent SDFs (see Supplementary Fig. 15) and show that the structure of the first solvation shell is highly ordered due to hydrogen bonds between the ligands and the solvent molecules.

A hydrogen bond is formed between an atom with a hydrogen bonded to it (the donor, D) and another atom (the acceptor, A). We used two geometric criteria to define hydrogen bonds: the distance between D and A, which should be less than 3.2 Å, and the D-H–A angle, which should be larger than 130 deg. Starting from the Fe-part of the FeRu molecule, we expect the lone pair of the nitrogen atoms of the cyano ligands to interact with the positive charge localized on the water hydrogens, so that the nitrogen is the acceptor and the water oxygen is the donor. Supplementary Fig. 15a shows that, when FeRu is in the ground state, the water hydrogens (H_w) and the water oxygens (O_w) are preferentially located at a distance of, respectively, 1.8 and 2.8 Å from the nitrogen atoms (N_{Fe}) of the equatorial and axial cyano ligands and at 0 and 75 degrees with respect to the C-N axis. The analysis of the coordination number for the N_{Fe}-O_w pairs (see Supplementary Fig. 18a) yields approximately 4.5 water molecules per cyano ligand in the first solvation shell. Supplementary Fig. 15b shows the distribution of the N_{Fe}–H_w-O_w angles, considering the water hydrogens in the first solvation shell. The

favorable angle for hydrogen bonding is 180 deg. and the distribution has a HWHM of approximately 12 deg. Based on these observations, we conclude that the two criteria for hydrogen bonding defined above are met in the case of cyano-water interactions.

Similar considerations and analysis can be made for the Ru-part of the FeRu molecule, where the nitrogen atom of the amine ligand is expected to be the donor and the water oxygen the acceptor. Supplementary Fig. 15c shows that water oxygen atoms are placed preferentially at a distance of 1.94 Å from the hydrogen atom of the amine and at 0 degrees with respect to the N_{Ru}-H axis. Considering the N_{Ru}-H bond length, we can extract a D-A distance of approximately 3 Å. The analysis of the coordination number for the H-O_w pairs (see Supplementary Fig. 18b) yields approximately 1 water molecules per each hydrogen atom of the amine ligand. Considering the water molecule in the first solvation shell, the peak and the HWHM of the N_{Ru}-H–O_w angular distribution are found, respectively, at 163 and 22 degrees (Supplementary Fig. 15d).

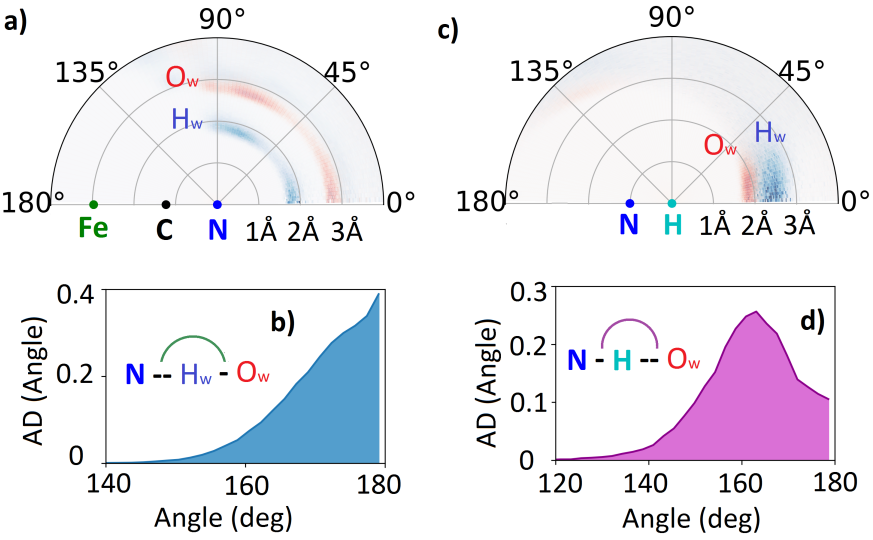

Supplementary Figure 15. SDFs calculated from the ground state equilibrium MD simulations of FeRu. a) SDF of the N_{Fe}-H_w (blue) and N_{Fe}-O_w (red) atom pairs as a function of distance r from the nitrogen atom and polar angle with respect to the C-N axis. b) Distribution of the N_{Fe}–H_w-O_w angles, considering the water hydrogens in the first solvation shell. c) SDF of the H-O_w (red) and H-H_w (blue) atom pairs as a function of distance r from the hydrogen atom and polar angle with respect to the N_{Ru}-H axis. d) N_{Ru}-H–O_w angular distribution considering the water oxygens in the first solvation shell.

6.2 Extended RDFs analysis

In this section, we present an extended analysis of the RDFs calculated from the non-equilibrium MD simulations.

Supplementary Figure 16 illustrates the temporal evolution of the N_{Ru}-O_w RDF obtained from the non-equilibrium simulations with t_{BET} = 60 fs. The position of the first solvation shell peak as a function of time is shown in Fig. 6c of the main text.

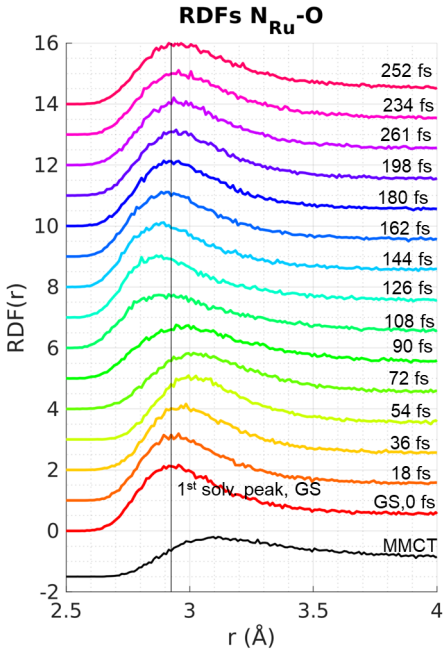

Supplementary Figure 16. N_{Ru}-O RDF as a function of time, with MMCT excitation at t=0 and BET at t = 60 fs. The RDF of the equilibrated MMCT state is shown for reference (black line). The position of the first solvation shell peak as a function of time is shown in Fig. 6c of the main text.

Supplementary Figure 17 illustrates that equivalent results are obtained when analyzing the temporal evolution of the N_{Fe}-H_w and N_{Fe}-O_w RDFs with respect to the solvent dynamics due to cyanide-water interactions, and of the N_{Ru}-O_w and H-O_w RDFs with respect to the solvent dynamics relative to the amine-water interactions.

In addition to the analysis presented in the main text, here we investigate the broadening of the first solvation shell peaks and the temporal evolution of the coordination number (calculated as in Supplementary Eq. 13) from the non-equilibrium simulations where the BET is initiated at 60 fs. Supplementary Fig. 18a shows the results obtained for the N_{Fe}-O_w RDFs. Upon MMCT, the first peak in the N_{Fe}-O_w RDFs broadens and there is a loss of hydrogens, indicating the diffusion of some water molecules of the first shell to the second shell. Upon BET, the FWHM and the number of molecules re-equilibrate and the the ground state values with an oscillatory pattern. Supplementary Fig. 18b show a similar evolution for the FWHM and the coordination number of the H-O_w RDFs as a function of time.

Finally, Supplementary Fig. 19 shows the results of the analysis of the N_{Fe}-H_w and H-O_w RDFs obtained from the five different non-equilibrium simulations. In particular panel a) and panel d) shows the time evolution of the first peak of the N_{Fe}-H_w and H-O_w RDFs, respectively, as a function of t_{BET}. We have fit each trace with a damped oscillator as for the analysis of the traces shown in Fig. 6b,c and the periods of the oscillations are reported in Supplementary Table 1.

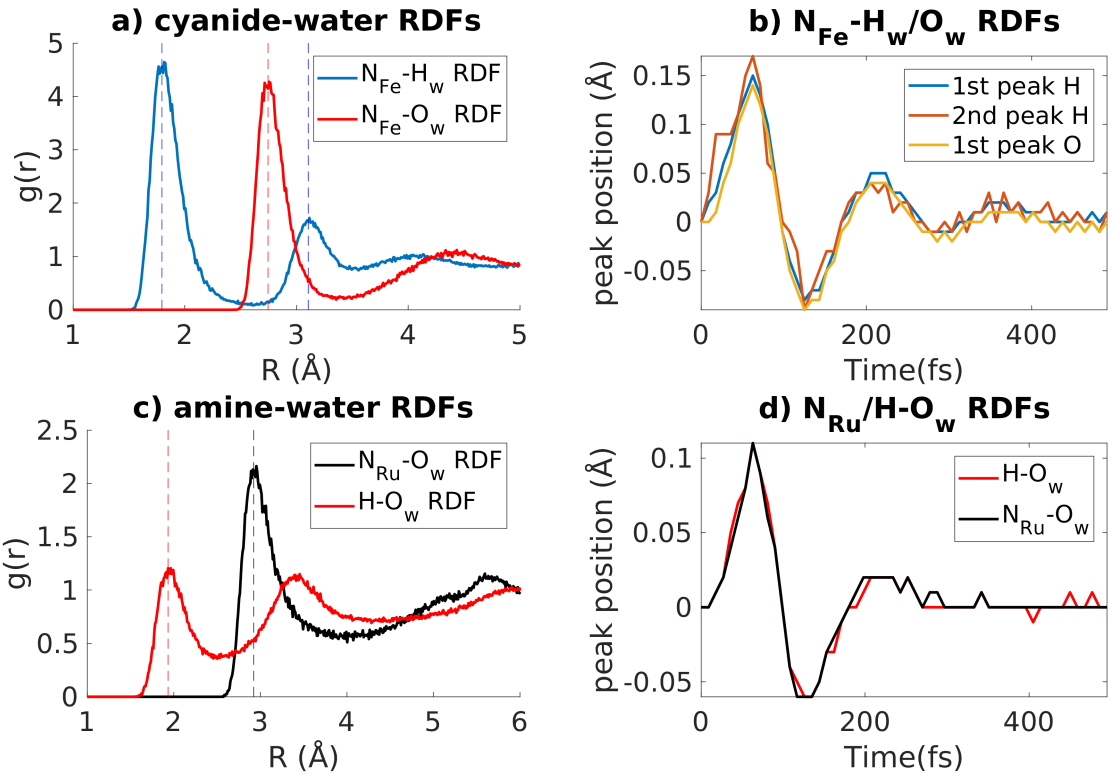

Supplementary Figure 17. a) N_{Fe}-H_w and N_{Fe}-O_w RDFs of solvated FeRu in the ground state. The dashed lines marked the positions of the relevant RDFs peaks. b) Temporal evolution of the RDFs peaks marked in panel (a) from non-equilibrium simulation where the BET is initiated at 60 fs. c) N_{Ru}-O_w and H-O_w RDFs of solvated FeRu in the ground state. d) Temporal evolution of the RDFs peaks marked in panel (c) from non-equilibrium simulation where the BET is initiated at 60 fs.

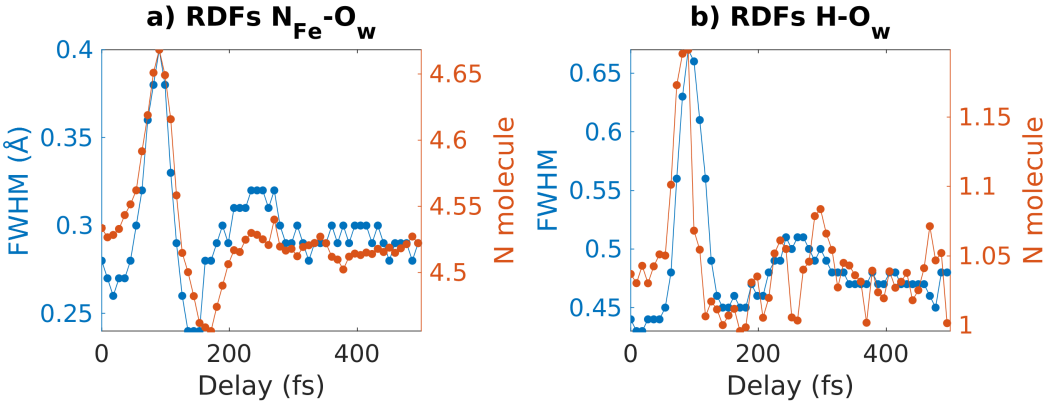

Supplementary Figure 18. Results from the analysis of the N_{Fe}-H_w (a) and H-O_w (b) RDFs obtained from out of equilibirum simulations (BET at t=60 fs). Specifically the plots show the values for the FWHM and the coordination number with respect to the first peak of the RDFs, as a function of time.

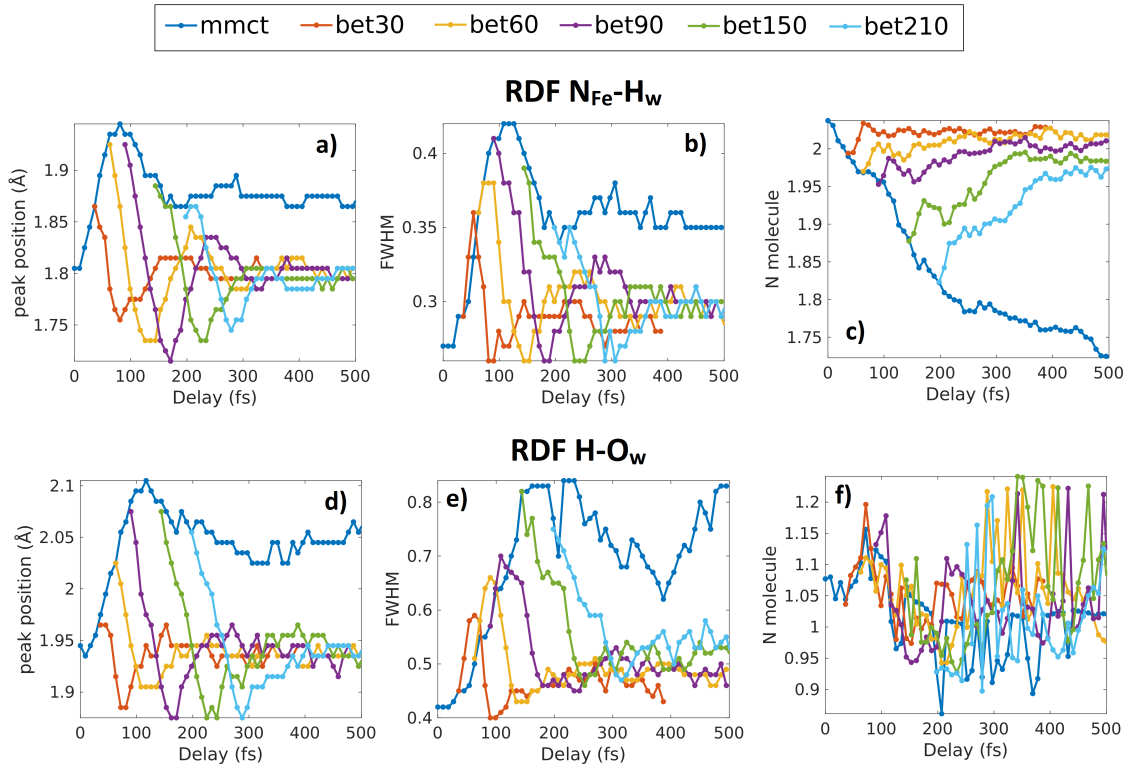

Supplementary Figure 19. From upper left to bottom right. a) Temporal evolution of the position of the first peak of the N_{Fe}-H_w RDFs as a function of BET times. b) Temporal evolution of the FWHM of the first peak of the N_{Fe}-H_w RDFs as a function of BET times. c) Temporal evolution of the coordination number calculated with respect to N_{Fe}-H_w RDFs as a function of BET times. d) Temporal evolution of the position of the first peak of the H-O_w RDFs as a function of BET times. e) Temporal evolution of the FWHM of the first peak of the H-O_w RDFs as a function of BET times. f) Temporal evolution of the coordination number calculated with respect to the H-O_w RDFs as a function of BET times.

6.3 Angular Distribution Functions analysis

In order to estimate the extent of rotational motion of the solvent molecules in the first solvation shell, we analyze the time evolution of N_{Fe}–H_w-O_w and the N_{Ru}-H–O_w angular distributions, shown in Supplementary Fig. 15c,d in the case of the ground state. Supplementary Fig. 20 shows that such distributions change only minimally upon MMCT and BET, signifying that rotational motions of the water molecules in the first solvation shell are negligible. This analysis, in combination of the RDFs analysis, indicate that the hydrogen bonds are weakened, but not broken, on the time scales of the MMCT and the BET events.

Supplementary Table 1. Fraction of the excited state molecules that decays to the GS at different BET times, and period of the oscillation of the first solvation shell obtained from the analysis of the N_{Fe}-H_w and H-O_w RDFs as a function of BET time (Supplementary Fig. 19a,d).

BET time (t_{BET})	Lin. Coeff.	Oscillation period	
		N_{Fe}-H_w	H-O_w
30 fs	34 %	164 ± 10 fs	NA
60 fs	27 %	161 ± 3 fs	175 ± 9 fs
90 fs	15 %	165 ± 4 fs	173 ± 7 fs
150 fs	15 %	178 ± 10 fs	230 ± 24 fs
210 fs	9 %	NA	276 ± 29 fs

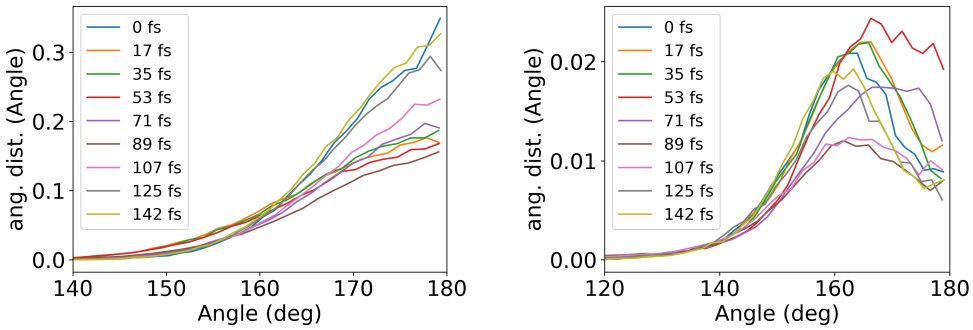

Supplementary Figure 20. N_{Fe}–H_w-O_w (left) and N_{Fe}–H_w-O_w (right) angular distributions as function of time, obtained from the non-equilibrium simulations with t_{BET} = 60 fs.

7 Solvation Energy

In order to relate our work to previous studies of solvation dynamics, we calculate the time-evolution of the solute–solvent interaction energy U (solvent response) from the MD simulations. Traditionally, the calculated solvent response has been directly compared to observables measured by optical experiments, such as time-resolved Stokes shift measurements. In these calculations, U comprises the electrostatic (Coulomb) and van Der Walls (Lennard-Jones) interactions and it is calculated considering water molecules within a 20 Å radius from the solute:

$$U = E_{\mathrm{C}} + E_{\mathrm{LJ}} \tag{4}$$

The Coulomb contribution is calculated as:

$$E_{\mathrm{C}} = \sum_{ij} k \frac{q_i q_j}{r_{ij}} \tag{5}$$

where i runs over all the solute atom, j over the solvent atom, k is the Coulomb constant and q_i and q_j the atomic partial charges of the solute and solvent atoms respectively.

The Lennard-Jones contribution is calculated as:

$$E_{\mathrm{LJ}} = \sum_{ij} \frac{A_{ij}}{r_{ij}^6} + \frac{B_{ij}}{r_{ij}^{12}} \tag{6}$$

where i runs over all the solute atom, j over the solvent atom, $A = (4\epsilon_{ij}\sigma_{ij}^6)^{1/2}$, $B = (-4\epsilon_{ij}\sigma_{ij}^{12})^{1/2}$, where ϵ_{ij} and σ_{ij} are obtained from the Lennard-Jones parameters of the atoms i and j through a geometric combining rule.

Following traditional studies of solvation dynamics, we calculate the solvent relaxation by computing both the equilibrium and the non-equilibrium solvent response function [12–14]. In the linear regime, the two solvent responses should show the same temporal evolution. The former is calculated from a MD equilibrium simulation of FeRu, where the dynamics is saved every 10 fs for a total of 100 ps:

$$C(t) = \frac{< \delta U(0)\delta U(t) >}{< \delta U(t)^2 >} \tag{7}$$

The latter is calculated from the non-equilibrium simulations:

$$S(t) = \frac{U(t_{\mathrm{START}}) - U(t_\infty)}{U(t_{\mathrm{START}}) - U(t_\infty)} \tag{8}$$

Specifically we use Supplementary Eq. 8 to calculate both a) the solvent response upon MMCT ($\mathrm{S_{MMCT}}$) with $\mathrm{t_{START}} = \mathrm{t_0}$ and using trajectories up to 1.5 ps, and b) the solvent response upon BET ($\mathrm{S_{BET}}$), using the non-equilibrium simulation where BET happens at t=60 fs ($\mathrm{t_{START}}$ = 60 fs) following by equilibration up to $\sim$ 400 fs.

Supplementary Fig. 21 summarises the results of this analysis. Supplementary Fig. 21a (bottom panel) shows that the solvent response upon MMCT can be considered approximately in the linear regime, since the time evolution of S(t) and C(t) are very similar to each other. On the contrary, Supplementary Fig. 21b (bottom panel) shows that $\mathrm{S_{BET}}$ cannot be described by C(t), which implies the failure of the linear response approximation in the case of the BET process in FeRu. S(t) shows a rapid decay followed mainly by high-frequency oscillations due to librational/rotational motions of water molecules, which are known to be the most efficient in relaxing the energy in dielectric solvation in water [15, 16]. S(t) then mainly reports on the long-range dipolar solvation due the dipole change upon electron transfer in FeRu. The failure of the linear response is likely due to the center-of-mass translational motions of the water molecules in the first solvation shell, that are uniquely captured by our time-resolved XSS experiments, and that are due to the weakening/strengthening of hydrogen bond interactions between the ligand and the water molecules upon MMCT/BET in FeRu. This is in agreement with previous computational studies that have shown that translational motions lead to breakdown of linear response in mechanical solvation [12, 14, 17].

From this analysis, the solvent reorganization energy is overestimated, as expected from the use of non-polarizable force fields [18, 19]. The energetic contributions of the water translational motions observed in our experiment to the overall solvent response to the electron transfer process in FeRu cannot be directly extracted from the XSS data. A reliable estimate of the solvent reorganization energy requires a full quantum-mechanical treatment of the solute–solvent interactions in the GS and MMCT state dynamics.

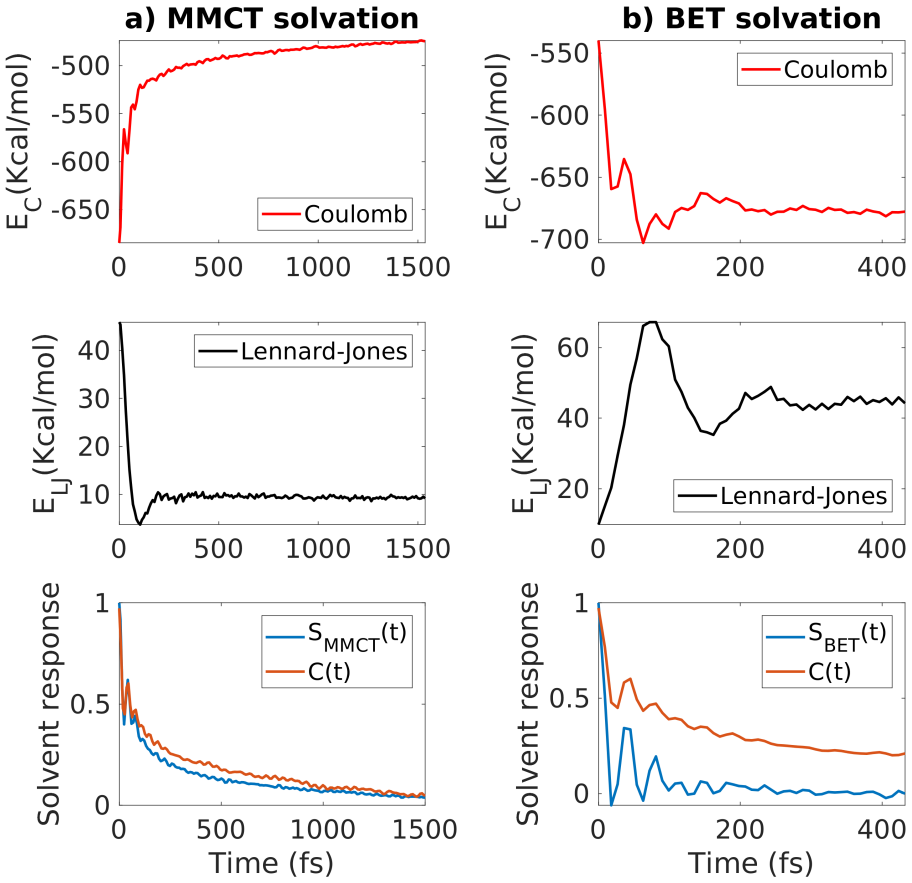

Supplementary Figure 21. Results of the analysis of the solute–solvent energy from the non-equilibrium MD simulations, as described in detail in the text. The bottom right panel shows that the time-evolution of the equilibrium solvent response is different than that of the non-equilibrium solvent response. This indicates the failure of linear response theory in describing the BET process in FeRu.

8 Anisotropic scattering signal

The anisotropy in the scattering signal arises from the combination of two factors: 1) the interaction of the linearly polarized pump laser pulse with the sample, which created an oriented excited state population of molecules, and 2) anisotropic structural changes that can be captured by femtosecond X-ray pulses. In the case of the MMCT transition in FeRu, the transition dipole is parallel to the Fe-Ru axis and the linearly polarized laser pulse preferentially excites the FeRu molecules with the transition dipole moment aligned with respect to laser polarization axis. Supplementary Figure 22a shows the anisotropic scattering signal measured upon 800 nm excitation of FeRu. The signal shows a low-Q positive feature, which decays in the 100 fs time scale, and that can arise from anisotropic changes in solute–solute and/or solute–solvent distances. The anisotropic scattering signal measured for $Q > 2$ Å^{-1} arises from changes in solvent–solvent atom pair distances. This signal is due to the Kerr effect, i.e. to

the impulsive response of the water molecules to the linearly polarized laser pulse, and it has been measured in separate experiments and in neat solvent [4, 20]. To simulate the anisotropic scattering signal, we calculate SDFs as a function of the polar angle with respect to the Fe-Ru axis from the MD simulations and we then use the following equation:

$$S_2(Q) = \sum_a N_a f_a(q)^2 + \sum_{a,b} f_a(Q) f_b(Q) 2\pi \frac{N_a(N_b - \delta_{a,b})}{V} \int_0^\infty dr r^2 j_2(Qr) \int_0^\pi d\theta \sin\theta g_{a,b}(r,\theta) P_2(\cos\theta) \tag{9}$$

where N_a is the number of atoms of type a, V is the volume of the box used in the MD simulations, f_a is the atomic form factor of atoms of type a, j_2 is the 2nd-order spherical-Bessel function, P_2 the 2nd-order Legendre polynomial, and θ is the angle between the vector connecting atom a and b and the main axis of symmetry of the molecule (i.e. the Fe-Ru axis, which corresponds to the transition dipole of the 800 nm excitation for this experiment). To our knowledge, this is the first time that anisotropic scattering signal are calculated with this formulation using results from MD simulations [21, 22]. Supplementary Fig. 22b shows the simulated scattering signal obtained from the solute–solvent SDFs calculated from the non-equilibirum simulations, following the same procedure used for the simulation of the isotropic part of the scattering data. The simulation reproduces the low-Q positive feature and its dynamics, though the magnitude of this feature is overestimated. We believe that changes in solute–solvent atom pair distances are anisotropic because of the asymmetric structure of the hydration shells surrounding the solute, as discussed above.

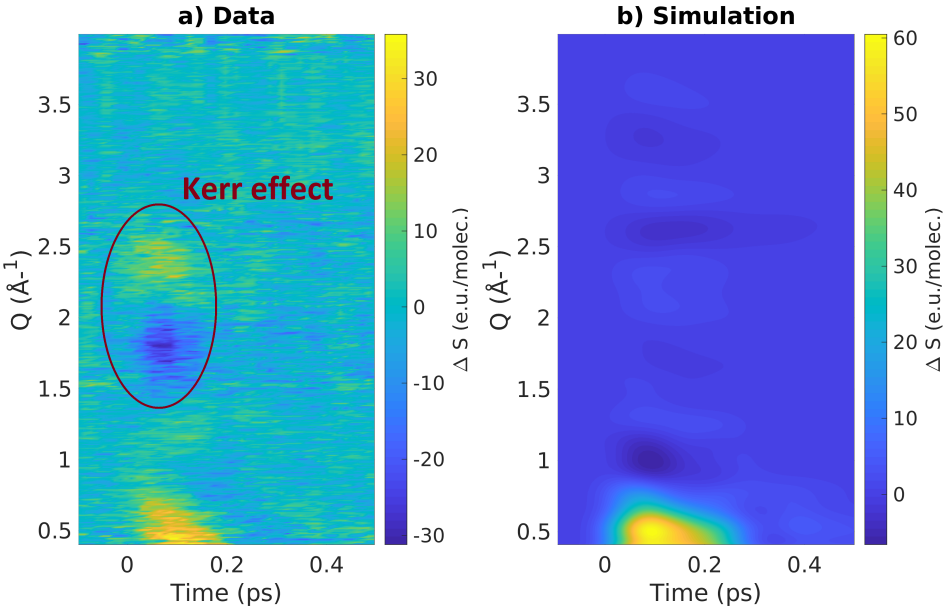

Supplementary Figure 22. Comparison between experimental and simulated anisotropic difference scattering signal.

9 Calculations details

9.1 QM/MM calculations

The 3D molecular model of the $Fe^{II}Ru^{III}$ complex was solvated in a cubic water box of side 53 Å consisting of 4992 water molecules with a density of $\sim$1 g/cm^3 using the preparation tools and a pre-prepared equilibrated bulk water template available in the NWChem computational chemistry software package [9, 23–25]. The solvation included placement of a single potassium cation (K+) in the water solvent to charge balance the 1- charged FeRu complex. The FeRu complex was designated the quantum mechanics (QM) region, and the water molecules with the K+ cation was designated the molecular mechanics (MM) region in the subsequent QM/MM simulations. The classical force-field used for the water molecules was the extended single point charge water model (SPC/E) of Berendsen *et al.* [26]. The single K+ cation was represented with the SPC/E-compatible K+ force field of Joung and Cheatham [27]. For the QM region, van der Waals parameters for the C, N, and H atoms were obtained from the general AMBER force-field (GAFF) set [28]. For the Fe and Ru atoms of the complex, which do not interact directly with the water solvent, the van der Waals parameters were assigned with the Fe2+ (feo) van der Waals parameters of the CLAYFF forcefield of Cygan *et al.* [29] to approximate the relatively short Fe/Ru-ligand van der Waals interactions. Lorentz-Berthelot mixing and AMBER 1-4 rules for non-bonding interactions apply. Following the preparation of the solvated system and assignment of force-field parameters, the system was optimized with the NWChem QM/MM module. The level of the quantum chemistry method used for the QM region was the hybrid PBE0 density functional [30,31] with the 6-311G** basis set for the light atoms, H, C, and N, [32] and the Stuttgart scalar relativistic basis set and effective core potentials (ECP) for Fe and Ru [33,34]. The SHAKE algorithm [35] was only applied to the water molecules to constrain the bond lengths and bond angle, as prescribed by the SPC/E potential. The cut-off for the Coulombic interactions was set to 1.2 nm. The QM/MM interaction zone surrounding the complex was set to 2.0 nm. Geometry optimization was performed cyclically with a maximum of 10 QM region Broyden-Fletcher-Goldfarb-Shanno (BFGS) iterations followed by a maximum of 3000 MM region steepest-descent (SD) iterations. This cycle was repeated for a maximum of 5 times until convergence. Following optimization, QM/MM dynamics were performed. Initially, the complex was held fixed and the water solvent was allowed to equilibrate over 10 ps with a time step of 2 fs and using the Berendsen's thermostat [36] for NVT simulations at 298.15 K. After this initial equilibration, the complex was allowed to equilibrate with the solvent for 1 ps and a time step of 0.25 fs. Following 1 ps, QM/MM dynamics of the entire system was ran for another 20 ps.

9.2 TDDFT calculations

For the time-dependent density functional theory (TDDFT) calculations of the $Fe^{II}Ru^{III}$ complex, clusters were extracted from the QM/MM trajectory. The clusters were constructed by taking the transition metal complex center as well as the 4Å thick shell of explicit water molecules surrounding the complex. This corresponds to clusters with a total of 238 atoms for the $Fe^{II}Ru^{III}$ complex, respectively. These clusters were

sufficiently large to capture the essential physics and tractable for our response calculations. These candidate clusters were optimized on the metal-metal charge-transfer (MMCT) excited-state to obtain the excited state geometries. These calculations were also performed with the NWChem program with the TDDFT module [37]. The QM calculation level was the same as described above. For the analysis described in the main text, the ground state corresponds to a structure where the electron is localized on Fe, while the excited state corresponds to a structure on the MMCT potential energy surface, where the electron is localized on Ru. Partial atomic charges for the solute atoms of a specific cluster are derived with the NWChem Electrostatic Potential (ESP) module using the corresponding electronic densities of the respective geometries. The GS structure of FeRu, as well as the ESP atomic partial charges used for the GS and MMCT states, are reported in Supplementary Table 2. The GS FeRu structural parameters are found in agreement with structural values obtained from Fe K-edge EXAFS studies of ferrocyanide in water [9,38], and with crystallographic studies of hexaammineruthenium(III) [39]. The calculated IR (Supplementary Fig. 23) and UV/Vis (Supplementary Fig. 24) spectra are also in good agreement with experiments.

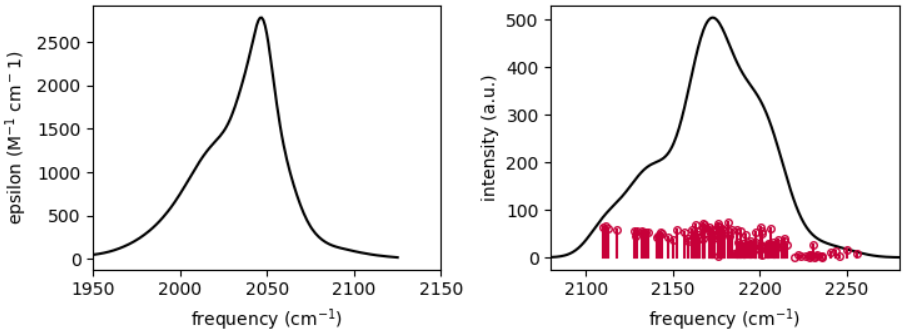

Supplementary Figure 23. Comparison between experimental (left) and simulated (right) IR spectra of the FeRu complex solvated in water. The simulated IR spectrum was calculated by averaging over 20 snaphots from the QM/MM trajectory. The simulated spectrum (black) has been obtained by applying a broadening of 10 cm^{-1} to the calculated discrete transitions (red).

9.3 MD simulations

For these simulations, we use the Desmond software package developed at D. E. Shaw Research [40]. The electrostatic potential (ESP) partial charges are used to describe the Coulombic interactions involving atoms of the solute, while other nonbonded interactions are modeled with the Lennard-Jones potential using parameters for the complex from the OPLS2005 force field [41]. The complex is frozen by applying harmonic positional restraints with force constant of 500 kcal/mol, and solvated in a cubic box with 60 Å side length containing 7065 water molecules using the TIP4P-Ew potential [42]. The propagation is performed in the NVT ensemble using a Nose-Hoover thermostat at 300 K [43], with a time step of 1 fs. The cut-off for the complete treatment of the coulombic interactions was set to 9 Å, and the Ewald summation method was used for

Supplementary Table 2. FeRu structure and ESP partial charges used for the non-equilibrium MD simulations.

Atom	x	y	z	GS ESP	ES ESP	Δ ESP
Fe	0.00000000	0.00000000	0.00000000	-1.561347	-0.665115	0.8962
C	1.94258795	0.08164614	0.14020343	0.430958	0.291769	-0.1392
N	3.10520417	0.13346716	0.20638222	-0.684770	-0.553406	0.1314
C	0.00266571	-1.71050308	0.88438509	0.634890	0.314967	-0.3199
N	-0.07525153	-2.81173174	1.29357301	-1.016455	-0.663797	0.3527
C	-0.10716525	0.94404203	1.68647007	0.508055	0.259374	-0.2487
N	-0.05838085	1.55215124	2.69407878	-0.948065	-0.641764	0.3063
C	0.01202453	1.67394058	-0.90763276	0.604412	0.385619	-0.2188
N	-0.04407769	2.70340941	-1.46770195	-1.021491	-0.716287	0.3052
C	0.23192906	-0.87972143	-1.71214525	0.621584	0.410027	-0.2116
N	0.44907824	-1.39676329	-2.74799361	-0.974079	-0.753563	0.2205
C	-1.89899629	-0.09859569	-0.20149820	0.675394	0.328772	-0.3466
N	-3.06054403	-0.15487717	-0.37261798	-1.087506	-0.744774	0.3427
Ru	5.10622901	0.18098331	0.54195815	1.355251	0.969218	-0.3860
N	7.16324427	0.19757098	1.00669098	-0.922178	-0.820412	0.1018
H	7.60343526	1.10998369	0.87575013	0.425439	0.297961	-0.1275
H	7.34708900	-0.04997395	1.98363225	0.433430	0.336822	-0.0966
H	7.66953139	-0.47628707	0.41016361	0.391469	0.321325	-0.0701
N	4.67340480	-0.71924103	2.42302825	-0.819100	-0.695964	0.1231
H	5.48128923	-0.91245090	3.01665257	0.379728	0.293769	-0.0860
H	4.03207680	-0.14296849	2.97292532	0.386379	0.300216	-0.0862
H	4.24624492	-1.63387608	2.29545710	0.336022	0.274690	-0.0613
N	5.51368585	1.02929581	-1.36477922	-0.882456	-0.789908	0.0925
H	5.01257799	0.46716811	-2.06011768	0.354294	0.290762	-0.0635
H	5.12603300	1.97902083	-1.40106131	0.381320	0.330364	-0.0510
H	6.49538257	1.04005526	-1.65665297	0.421962	0.290043	-0.1319
N	5.32139168	-1.70500847	-0.38880686	-0.811781	-0.620251	0.1915
H	4.66621164	-1.76899455	-1.17320483	0.372277	0.304633	-0.0676
H	6.25969324	-1.81520917	-0.78103438	0.360183	0.224618	-0.1356
H	5.18379574	-2.49683390	0.25139493	0.396879	0.278713	-0.1182
N	4.86068770	2.11770342	1.37327112	-0.934768	-0.875018	0.0598
H	4.27157833	2.64715675	0.71669804	0.402692	0.368372	-0.0343
H	4.39132780	2.09738349	2.28385473	0.372733	0.364621	-0.0081
H	5.74344302	2.62613103	1.41427021	0.418643	0.303605	-0.1150

the long-range electrostatic interaction. The RDFs are sampled in 0.01 Å using the VMD software [44].

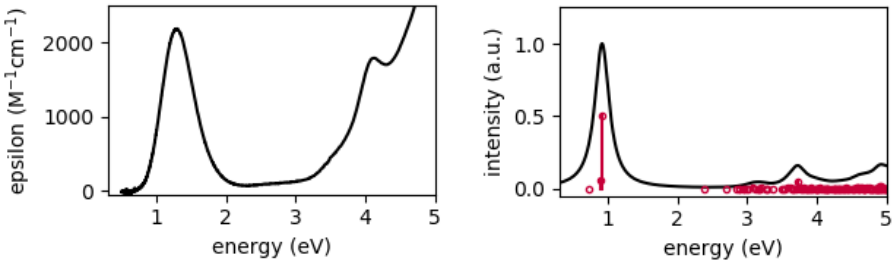

Supplementary Figure 24. Comparison between experimental (left) and simulated (right) UV/Vis spectra of the FeRu complex solvated in water. The simulated spectrum (black) has been obtained by applying a broadening of 0.25 eV to the calculated discrete transitions (red).

9.4 Calculation of Spacial Distribution Functions

We start by counting the average number of j neighbors at distance r around an i particle and at an angle θ from a given axis. Such histograms are constructing using 0.025 Å radial bins and 1.8° angular bins:

$$hist_{ij}(\mathrm{r},\theta) = \sum_{i}^{N_i}\sum_{j\neq i}^{N_j} \langle \delta(|\mathbf{r}_i - \mathbf{r}_j| - r)\delta(\theta_{ij} - \theta)\rangle \tag{10}$$

where N_i and N_i are the number of atoms i and j respectively. We then normalize such histogram by the solid angle and the density $\rho = N_i \cdot (N_j - \delta_{ij}) \cdot \mathrm{V}^{-1}$ (where V is the volume of the system) to obtain spatial distribution function g(r, θ):

$$\mathrm{g(r,}\ \theta) = \frac{hist_{ij}(\mathrm{r},\theta)}{\rho \cdot \pi \mathrm{r}^2 d\mathrm{r} \sin\theta d\theta} \tag{11}$$

We can obtain Radial Distribution Functions (RDFs) g(r) by integrating over the angular variable:

$$\mathrm{g(r)} = \frac{1}{2}\int_0^{2\pi} g(r,\theta) sin\theta d\theta \tag{12}$$

The coordination number c_{ij} (i.e. the number of molecule j in the first solvation shell of atom i) with the following equation:

$$\mathrm{c}_{ij} = 4\pi\rho \int_0^{R_1} g_{ij}(\mathrm{r})\mathrm{r}^2 d\mathrm{r} \tag{13}$$

where R_1 is the first minimum of g_{ij}.

9.5 Calculation of Angular Distributions

Histograms of the D-H–A angles, where D and A are the donor and the acceptor atom involved in the hydrogen bonds, are calculated for each collection of MD frames relative to the same time-delay. In the case of the $\mathrm{N_{Fe}}$–$\mathrm{H_w}$-$\mathrm{O_w}$ angles, for each frame and for each equatorial and axial $\mathrm{N_{Fe}}$: a) the hydrogens within the boundary of

the first solvation shell for that specific N_{Fe} are identified, b) the oxygen bounded to each of the hydrogen are identified, c) the N_{Fe}–H_w-O_w angles are calculated and binned. Shell boundary (FWHM) are taken from the analysis of the N_{Fe}–H_w RDFs, as described above. In the case of the N_{Ru}-H–O_w angles, for each frame and for each H : a) the oxygen within the FWHM of the first solvation shell for that specific H are identified, b) the N_{Ru}-H-O_w angles are calculated and binned. The obtained histogram are weighted by the solid angle of the angular bins and the area of the so-otained angular distributions are, as a result, proportional to the number of atoms considered, i.e. the number of hydrogens/oxygens within the shell boundary. Supplementary Fig. 20 shows the angular distribution obtained from the non-equilibrium simulation as a function of time (MMCT at t=0 and BET at t=60 fs).

References

[1] Vogler, A. & Kisslinger, J. Photosubstitution of pentaamminechlororuthenium(iii) hexacyanoruthenate(ii) following outer-sphere intervalence excitation. *Journal of the American Chemical Society* **104**, 2311–2312 (1982).

[2] Kjær, K. S. *et al.* Introducing a standard method for experimental determination of the solvent response in laser pump, x-ray probe time-resolved wide-angle x-ray scattering experiments on systems in solution. *Phys. Chem. Chem. Phys.* **15**, 15003–15016 (2013).

[3] Biasin, E. *et al.* Anisotropy enhanced X-ray scattering from solvated transition metal complexes. *Journal of Synchrotron Radiation* **25**, 306–315 (2018).

[4] Biasin, E. *et al.* Femtosecond x-ray scattering study of ultrafast photoinduced structural dynamics in solvated co(terpy)2. *Phys. Rev. Lett.* **117**, 013002 (2016).

[5] Son, D. H., Kambhampati, P., Kee, T. W. & Barbara, P. F. Femtosecond multi-color pump−probe study of ultrafast electron transfer of [(nh3)5ruiiincruii(cn)5]- in aqueous solution. *The Journal of Physical Chemistry A* **106**, 4591–4597 (2002).

[6] Haldrup, K. *et al.* Ultrafast x-ray scattering measurements of coherent structural dynamics on the ground-state potential energy surface of a diplatinum molecule. *Phys. Rev. Lett.* **122**, 063001 (2019).

[7] Kunnus, K. *et al.* Vibrational wavepacket dynamics in fe carbene photosensitizer determined with femtosecond x-ray emission and scattering. *Nature Communications* **11**, 634 (2020).

[8] Chergui, M. Ultrafast photophysics and photochemistry of iron hexacyanides in solution: Infrared to x-ray spectroscopic studies. *Coordination Chemistry Reviews* **372**, 52 – 65 (2018).

[9] Ross, M. *et al.* Comprehensive experimental and computational spectroscopic study of hexacyanoferrate complexes in water: From infrared to x-ray wavelengths. *The Journal of Physical Chemistry B* **122**, 5075–5086 (2018).

[10] Reid, P. J., Silva, C., Barbara, P. F., Karki, L. & Hupp, J. T. Electronic coherence, vibrational coherence, and solvent degrees of freedom in the femtosecond spectroscopy of mixed-valence metal dimers in h2o and d2o. *The Journal of Physical Chemistry* **99**, 2609–2616 (1995).

[11] Kjær, K. S. *et al.* Finding intersections between electronic excited state potential energy surfaces with simultaneous ultrafast x-ray scattering and spectroscopy. *Chem. Sci.* **10**, 5749–5760 (2019).

[12] Fonseca, T. & Ladanyi, B. M. Breakdown of linear response for solvation dynamics in methanol. *The Journal of Physical Chemistry* **95**, 2116–2119 (1991).

[13] Heid, E., Moser, W. & Schröder, C. On the validity of linear response approximations regarding the solvation dynamics of polyatomic solutes. *Phys. Chem. Chem. Phys.* **19**, 10940–10950 (2017).

[14] Aherne, D., Tran, V. & Schwartz, B. J. Nonlinear, nonpolar solvation dynamics in water: The roles of electrostriction and solvent translation in the breakdown of linear response. *The Journal of Physical Chemistry B* **104**, 5382–5394 (2000).

[15] Jimenez, R., Fleming, G. R., Kumar, P. V. & Maroncelli, M. Femtosecond solvation dynamics of water. *Nature* **369**, 471–473 (1994).

[16] Stratt, R. M. & Maroncelli, M. Nonreactive dynamics in solution: The emerging molecular view of solvation dynamics and vibrational relaxation. *The Journal of Physical Chemistry* **100**, 12981–12996 (1996).

[17] Bragg, A. E., Cavanagh, M. C. & Schwartz, B. J. Linear response breakdown in solvation dynamics induced by atomic electron-transfer reactions. *Science* **321**, 1817–1822 (2008).

[18] Stöhr, M. & Tkatchenko, A. Quantum mechanics of proteins in explicit water: The role of plasmon-like solute-solvent interactions. *Science Advances* **5** (2019).

[19] Vladimirov, E., Ivanova, A. & Rösch, N. Effect of solvent polarization on the reorganization energy of electron transfer from molecular dynamics simulations. *The Journal of Chemical Physics* **129**, 194515 (2008).

[20] Kjær, K. S. *et al.* Finding intersections between electronic excited state potential energy surfaces with simultaneous ultrafast x-ray scattering and spectroscopy. *Chem. Sci.* **10**, 5749–5760 (2019).

[21] Lorenz, U., Møller, K. B. & Henriksen, N. E. On the interpretation of time-resolved anisotropic diffraction patterns. *New Journal of Physics* **12**, 113022 (2010).

[22] Dohn, A. O. *et al.* On the calculation of x-ray scattering signals from pairwise radial distribution functions. *Journal of Physics B: Atomic, Molecular and Optical Physics* **48**, 244010 (2015).

[23] Aprà, E. *et al.* Nwchem: Past, present, and future. *The Journal of chemical physics* **152**, 184102 (2020).

[24] Lopata, K., Van Kuiken, B. E., Khalil, M. & Govind, N. Linear-response and real-time time-dependent density functional theory studies of core-level near-edge x-ray absorption. *Journal of Chemical Theory and Computation* **8**, 3284–3292 (2012).

[25] Van Kuiken, B. E. *et al.* Simulating ru l3-edge x-ray absorption spectroscopy with time-dependent density functional theory: Model complexes and electron localization in mixed-valence metal dimers. *The Journal of Physical Chemistry A* **117**, 4444–4454 (2013).

[26] Berendsen, H. J. C., Grigera, J. R. & Straatsma, T. P. The missing term in effective pair potentials. *The Journal of Physical Chemistry* **91**, 6269–6271 (1987).

[27] Joung, I. S. & Cheatham, T. E. Determination of alkali and halide monovalent ion parameters for use in explicitly solvated biomolecular simulations. *The Journal of Physical Chemistry B* **112**, 9020–9041 (2008).

[28] Wang, J., Wolf, R. M., Caldwell, J. W., Kollman, P. A. & Case, D. A. Development and testing of a general amber force field. *Journal of Computational Chemistry* **25**, 1157–1174 (2004).

[29] Cygan, R. T., Liang, J.-J. & Kalinichev, A. G. Molecular models of hydroxide, oxyhydroxide, and clay phases and the development of a general force field. *The Journal of Physical Chemistry B* **108**, 1255–1266 (2004).

[30] Perdew, J. P., Ernzerhof, M. & Burke, K. Rationale for mixing exact exchange with density functional approximations. *The Journal of Chemical Physics* **105**, 9982–9985 (1996).

[31] Adamo, C. & Barone, V. Toward reliable density functional methods without adjustable parameters: The pbe0 model. *The Journal of Chemical Physics* **110**, 6158–6170 (1999).

[32] Krishnan, R., Binkley, J. S., Seeger, R. & Pople, J. A. Self-consistent molecular orbital methods. xx. a basis set for correlated wave functions. *The Journal of Chemical Physics* **72**, 650–654 (1980).

[33] Dolg, M., Wedig, U., Stoll, H. & Preuss, H. Energy-adjusted ab initio pseudopotentials for the first row transition elements. *The Journal of Chemical Physics* **86**, 866–872 (1987).

[34] Andrae, D., Häußermann, U., Dolg, M., Stoll, H. & Preuß, H. Energy-adjusted ab initio pseudopotentials for the second and third row transition elements. *Theoretica chimica acta* **77**, 123–141 (1990).

[35] Ryckaert, J.-P., Ciccotti, G. & Berendsen, H. J. Numerical integration of the cartesian equations of motion of a system with constraints: molecular dynamics of n-alkanes. *Journal of Computational Physics* **23**, 327 – 341 (1977).

[36] Berendsen, H. J. C., Postma, J. P. M., van Gunsteren, W. F., DiNola, A. & Haak, J. R. Molecular dynamics with coupling to an external bath. *The Journal of Chemical Physics* **81**, 3684–3690 (1984).

[37] Silverstein, D. W., Govind, N., Van Dam, H. J. & Jensen, L. Simulating one-photon absorption and resonance raman scattering spectra using analytical excited state energy gradients within time-dependent density functional theory. *Journal of chemical theory and computation* **9**, 5490–5503 (2013).

[38] Hayakawa, K. *et al.* Full quantitative multiple-scattering analysis of x-ray absorption spectra: application to potassium hexacyanoferrat(ii) and -(iii) complexes. *Journal of the American Chemical Society* **126**, 15618–15623 (2004).

[39] Stynes, H. C. & Ibers, J. A. Effect of metal-ligand bond distances on rates of electron-transfer reactions. crystal structures of hexaammineruthenium(ii) iodide, [ru(nh3)6]i2, and hexaammineruthenium(iii) tetrafluoroborate, [ru(nh3)6][bf4]3. *Inorganic Chemistry* **10**, 2304–2308 (1971).

[40] Bowers, K. J. *et al.* Scalable algorithms for molecular dynamics simulations on commodity clusters. In *SC '06: Proceedings of the 2006 ACM/IEEE Conference on Supercomputing*, 43–43 (2006).

[41] Jorgensen et al., W. L. Development and testing of the opls all-atom force field on conformational energetics and properties of organic liquids. *Journal of the American Chemical Society* **118**, 11225–11236 (1996).

[42] Horn, H. W. *et al.* Development of an improved four-site water model for biomolecular simulations: Tip4p-ew. *The Journal of Chemical Physics* **120**, 9665 (2004).

[43] Martyna, G. J., Klein, M. L. & Tuckerman, M. Nosé–hoover chains: The canonical ensemble via continuous dynamics. *The Journal of Chemical Physics* **97**, 2635–2643 (1992).

[44] Humphrey, W., Dalke, A. & Schulten, K. VMD – Visual Molecular Dynamics. *Journal of Molecular Graphics* **14**, 33–38 (1996).